Friedrich-Alexander-Universität
Faculty of Sciences

Bachelor's thesis

in physics

Modeling young Galactic stellar clusters from Gaia using binary population synthesis code COMPAS

Anna Rosensaft

Supervisor: Dr. Alison Mitchell
Erlangen Centre of Astroparticle Physics (ECAP)

Submission date: 25-06-2026

Abstract

A large fraction of the stars in our Galaxy are grouped in stellar clusters. Young stellar clusters, in particular, host the most massive stars in the Galaxy and, due to their strong winds, are considered as possible particle accelerators, contributing to the cosmic ray flux.

The identification of Galactic stellar clusters was revolutionized by the latest data releases of the *Gaia* mission (DR2 and DR3). However, estimating the mass and wind properties of clusters remains a challenging task due to the incompleteness of observational data.

The aim of this thesis is to simulate young ($< 30\,\mathrm{Myr}$) open clusters observed by *Gaia* by using the binary population synthesis code COMPAS to evaluate cluster properties such as mass, stellar wind or supernova and Wolf-Rayet star counts. To test how well population synthesis can reproduce actual clusters, the quantities of simulated clusters are compared to observational catalogues.

It was found that, depending on the range of the initial mass function, the mass of simulated clusters could be estimated within a $\sim 20\%$ accuracy to the literature values. Simulated cluster masses correlate the most with the literature catalogues that were used to normalize the corresponding simulation (Pearson $r \approx 0.95 - 0.99$), while comparisons with other catalogues have systematic offsets. Wind properties track, in general, the trends in cluster mass, while simulated supernova and Wolf-Rayet star counts exceed catalogue values by several orders of magnitude across all simulated populations.

Contents

1 Introduction & Motivation

The observation of stellar clusters goes back to Galileo Galilei. In his *Siderius Nuncius* (Sidereal Messenger, 1610) he describes the Galaxy as “nothing else than a congeries of innumerable stars distributed in clusters” [1]. Today, several centuries later, many aspects of stellar clusters still remain unknown, making them the subject of modern research. Stellar clusters can have various forms, sizes and ages, the oldest of them setting a lower limit of the age of the Universe [2]. Young clusters are ideal for studying the formation of stars and their effect on the interstellar medium [3]. Apart from that, the high-energy astroparticle physics community is interested in the most massive young clusters, since they are considered to be possible particle accelerators [4]. In particular, the Large High Altitude Air Shower Observatory (LHAASO) has detected the highest energy that was ever observed in γ-ray astronomy ($\sim 1\text{PeV} = 10^{15}\text{eV}$) in the Cygnus Cocoon, a Galactic stellar cluster [5]. A major challenge in astroparticle physics is to identify the origin and physical nature of such ultrahigh-energy sources. Since supernova remnants cannot account for energies in that regime, alternative sources such as pulsar wind nebulae [6] and young stellar clusters [7][4] have been proposed as possible sources. The energy budget available for particle acceleration in a cluster is set by its total mass and power of stellar winds [7], therefore, it is crucial to accurately characterize the physical parameters of young stellar clusters.

The most accurate survey of the Milky Way to this day was performed by the *Gaia* satellite [8] of the European Space Agency (ESA). The astrometric and photometric data of about two billion sources reported by *Gaia* improved the understanding of the structure and evolution of the Galaxy. The observational data serves as source for the identification of known as well as newly formed clusters and their evolution [9]. Stellar cluster catalogues based on *Gaia* observations are, among others, presented by Cantat-Gaudin et al. [10] and Hunt & Reffert [11]. The latter covers 7167 stellar clusters and represents the largest search of open clusters to date. Despite advances in observational accuracy, the identification of stellar clusters remains a difficult task. Observational challenges such as the detection of faint stars, unresolved binaries or the blending of close sources create selection effects that reduce the completeness and reliability of the data [11]. As a result, estimates of the total mass and number of member stars carry large uncertainties. Methods that infer cluster parameters from observational data must therefore rely on theoretical models to account for this incompleteness. Numerical simulations of stellar clusters offer a way to test the consistency of these methods: since simulated clusters are not subject to the same limitations as observations, it is possible to estimate cluster parameters while accounting for components that are otherwise not observed.

The aim of this study is to simulate young open stellar clusters based on *Gaia* observations in order to estimate their physical parameters, such as total mass and wind mass-loss rate, and compare them to the literature. For this purpose, the binary population synthesis code COMPAS (Compact Object Mergers: Population Astrophysics and Statistics) [12] is used. Binary and stellar population synthesis codes (BPS and SPS) have been developed to study the structure and evolution of stars. SPS codes use basic stellar equations (mass continuity, hydrostatic equilibrium, energy conservation and energy transport) to calculate the structure and evolution of stars [13]. This way, a lot of observed phenomena can be reproduced and studied in detail. SPS codes require three main inputs: (1) a stellar evolution theory specified by isochrones, (2) stellar spectral libraries, and (3) an Initial Mass Function (IMF) that sets the number of stars at each mass [14]. BPS codes additionally include the evolution of binary systems, which can lead to the formation of exotic phenomena such as Double Compact Objects (DCOs) or mergers [15][12]. Unlike SPS, BPS codes can evolve a large number of stars simultaneously, which makes it possible to predict the behaviour of stellar clusters or even entire galaxies.

The BPS code COMPAS is based on the same principles as other BPS codes such as StarTrack [16], COSMIC [17], and BSE [18], however, it was specifically designed to evolve very large populations of binaries in an efficient way. For example, a few hundred binaries can be evolved in seconds on a modern laptop and million binaries in a few CPU hours [12]. This makes COMPAS suitable for simulations of populations on the cluster-scale. All simulations in this study were performed with COMPAS version 03.29.00, available at `https://github.com/TeamCOMPAS/COMPAS/`.

This work is structured as follows. Section 2 describes theoretical aspects of stellar and binary evolution and the physics of stellar clusters. Section 3 then introduces the BPS code COMPAS and how it can be used to simulate populations consistent with stellar clusters. Section 4 presents the simulation of young Galactic open clusters based on *Gaia*'s observational data, discusses various aspects of the simulation using selected example clusters and compares simulated cluster parameters to the literature. Finally, Section 5 concludes the work and gives an outlook on further research opportunities.

2 Stellar Evolution & Stellar Cluster Physics

In order to understand the evolution of stellar clusters and their properties, one should first understand the way single stars evolve.

2.1 Fundamental Properties of Stars

Stars are gaseous spheres composed primarily of hydrogen and helium [19][1]. For a body to be classified as a star it must satisfy two conditions: (a) it has to be bound by self-gravity, and (b) its radiated energy must be supplied by an internal source. The main source of stellar radiation is nuclear fusion, which gradually alters the star's structure and composition over time. The total amount of energy radiated by a star per unit time is given by its luminosity

$$L = 4\pi R_\star^2 \sigma_{\mathrm{SB}} T_{\mathrm{eff}}^4 \,, \tag{2.1}$$

where $R_\star$ is the stellar radius and σ_{SB} the Stefan-Boltzmann constant. The temperature of a star is characterized by the effective temperature T_{eff}, defined as the temperature that a blackbody would need to have in order to emit the same power per unit area as the star. From this, the stellar flux F can be defined as

$$F = \sigma_{\mathrm{SB}} T_{\mathrm{eff}}^4 \,. \tag{2.2}$$

Stellar masses typically range from $0.08\,\mathrm{M}_\odot$ to $150\,\mathrm{M}_\odot$, where $\mathrm{M}_\odot$ is the mass of the Sun. Objects below the limit of $0.08\,\mathrm{M}_\odot$ [20] cannot sustain hydrogen fusion efficiently, but will fuse deuterium as an internal energy source. Such objects, also known as brown dwarfs, mostly shine by reflecting light rather than by radiating it themselves. Stars exceeding the upper mass limit of $150\,\mathrm{M}_\odot$ [21], on the other hand, would become too unstable due to their strong driven stellar winds.

Another defining stellar parameter is the chemical composition, described by the mass fractions X, Y and Z of hydrogen, helium and all heavier elements, respectively. Z is often called metallicity with $X + Y + Z = 1$ [19].

Based on their temperature, stars are classified into spectral types following the *Harvard* classification scheme "OBAFGKM" [22], ordered from hottest to coolest. The brightness of stars can be expressed through its *apparent magnitude* m, or alternatively, the *absolute magnitude* M, which is defined as the magnitude measured at a distance of 10 parsec. The difference between them, known as the distance modulus, is given as

$$m - M = 5\log_{10}(d) - 5 \,, \tag{2.3}$$

where d is the star's distance measured in parsec.

The interior structure of stars is governed by a set of differential equations that describe mass continuity, hydrostatic equilibrium, energy production, and energy transport [23]. Together, these equations form an underdetermined system that can be coupled through the *equation of state*, which relates density, temperature, and pressure.

[1] The following chapters on the properties and evolution of stars are mainly based on the textbooks of Prialnik [19] and Carroll & Ostlie [20], if not otherwise indicated.

The primary source of stellar energy is nuclear fusion. In this process hydrogen is converted into helium, which can occur through different reaction chains, namely the proton-proton (*pp*) chain and CNO cycle. The *pp*-chain first fuses two protons into deuterium, which then builds up to ^3He and ^4He. The CNO cycle involves carbon, nitrogen and oxygen nuclei to convert hydrogen into helium. The energy generation rate of the *pp*-chain scales as $\propto T^4$, while the CNO cycle scales as $\propto T^{20}$ near $T = 1.5 \cdot 10^7\,\mathrm{K}$ [20]. Due to this much steeper temperature dependence, the CNO cycle dominates in more massive stars with hotter cores, while the *pp*-chain is dominant in the cooler cores of low-mass stars. Stars with masses $\gtrsim 0.5 M_\odot$ have cores that become hot and dense enough for helium burning to ignite via the triple-alpha reaction once all of the hydrogen in the core has been used up. This process converts ^4He into ^{12}C and has an even steeper temperature dependence ($\propto T^{40}$ [20]). Since more massive stars have higher central pressures, they burn hydrogen more rapidly than low-mass stars. As a result, the age of a star $\tau_\star$ is inversely proportional to its mass $M_\star$, meaning that more massive stars have shorter lifetimes.

2.2 Evolution of Stars in a Nutshell

The theory of stellar evolution presented here is based on several fundamental assumptions [19]. First, stars are treated as isolated objects in space, such that their evolution depends only on their own initial conditions and is unaffected by other objects. Second, the initial composition of a star is assumed to be homogeneous and overall similar across all stars. Under these assumptions, the parameter that governs a star's evolution is its mass.

2.2.1 Pre-Main Sequence & Zero-Age Main Sequence

The formation of stars happens from the gravitational collapse of interstellar gas clouds. As the material collapses, the pressure rises and causes the temperature and density to increase as well. Once the pressure becomes high enough to slow the collapse to a quasi-static one, hydrostatic equilibrium is established for the first time, marking the formation of pre-main-sequence stars. Once the core temperature is sufficient to ignite nuclear reactions, hydrogen burning begins and the star reaches the Zero-Age Main Sequence (ZAMS). The ZAMS phase is a convenient starting point for stellar evolution models, since convective mixing during the pre-main-sequence phase erases any dependence on the star's formation history. Consequently, ZAMS stars can be treated as chemically homogeneous, independent of their initial conditions [24].

2.2.2 Main Sequence & Post-Main Sequence

Stars spend most of their lifetimes on the Main Sequence (MS) converting hydrogen to helium in their cores and reach the end of the MS phase once the central hydrogen is exhausted. The further evolution of the star depends on its mass. Low-mass ($0.5 \lesssim M \lesssim 2.3\,M_\odot$ [20]) and intermediate-mass ($2.3 \lesssim M \lesssim 8\,M_\odot$ [20]) stars evolve into White Dwarfs (WDs), while massive stars ($> 8\,M_\odot$) undergo a core-collapse supernova, leaving behind a Neutron Star (NS) or Black Hole (BH). Stars of very low mass ($< 0.5\,M_\odot$) evolve so slowly that they show no significant evolution over the age of the Universe.

The evolution of a star can be visualized using a Hertzsprung-Russell (HR) diagram, which plots effective temperature $T_{\rm eff}$ against luminosity $L_\star$. A schematic example is shown in Fig. 2.1, tracing the evolutionary tracks of stars with masses $1\,\mathrm{M}_\odot, 5\,\mathrm{M}_\odot$ and $25\,\mathrm{M}_\odot$. The evolution of a $1\,\mathrm{M}_\odot$ star can be described as follows: The star spends about 2/3 of its life on the MS (1-2). The exhaustion of central hydrogen is marked as *turn-off point* (2), after which the core begins to contract, while hydrogen continues to burn in a surrounding shell (2-3). During this phase, the luminosity increases, the effective temperature decreases, and the envelope expands. The decreasing temperature causes the formation of a convection zone near the surface, marking the "first dredge-up". The convection zone deepens as the star follows the Red Giant Branch (RGB) (4-5), transporting material from the interior of the star to the surface. At the top of the RGB the central temperature and density become sufficient to ignite the triple-alpha process. In low-mass stars, the electron-degenerate core ignites helium burning accompanied by a helium flash (5). The star then moves onto the Horizontal Branch (HB) (6), burning helium in its core and hydrogen in a surrounding shell. Once central helium is exhausted, a helium-burning shell forms around a carbon-oxygen core, marking the begin of the Asymptotic Giant Branch (AGB) (7-8). The AGB is characterized by strong stellar winds driven by the high radiation pressure in the envelope with mass-loss rates reaching up to $10^{-4}\,\mathrm{M}_\odot\,\mathrm{yr}^{-1}$ [20]. Following a final phase of mass loss, accompanied by thermal pulses (8), the remaining envelope is ejected, leaving behind the compact carbon-oxygen core as a WD. The expelled envelope, visible as a glowing shell around the WD progenitor, is known as Planetary Nebula (PN) (8-9). It reveals the products of the star's earlier nuclear burning, made visible through fluorescence [20].

WDs have no internal nuclear energy source. Their carbon-oxygen cores are supported against gravity by the pressure of degenerate electrons. The maximum mass of a WD is determined by the *Chandrasekhar* limit $M_{\rm Ch} \approx 1.44\,\mathrm{M}_\odot$ [25]. Above this limit, degeneracy pressure can no longer balance the self-gravity. The WD cools by radiating away its remaining thermal energy, essentially behaving like a hot piece of metal.

The evolution of massive stars has rather different characteristics. Since the central pressure is insufficient to produce a degenerate core, helium burning is ignited without a helium flash. Mass loss, in contrast, plays a far more important role for massive stars and remains one of the largest sources of uncertainty in describing their evolution [26][27][28]. Massive stars move along lines of constant luminosities across the HR diagram. Unlike lower-mass stars, nuclear fusion in massive stars continues beyond helium burning, proceeding with carbon and oxygen burning and the fusion of heavier elements. Each burning stage leaves behind a corresponding shell, giving the star an onion-like structure by the end of its life. Fusion finally halts when an iron core has formed, which then collapses (10), triggering a supernova explosion (11).

The high mass loss during the MS phase leaves massive stars with envelopes that consist mainly of helium. Such stars that additionally have very high luminosities and unusually strong emission lines are classified as Wolf-Rayet (WR) stars. These stars are extremely hot ($T_{\rm eff} \sim 25\,000\,\mathrm{K} - 100\,000\,\mathrm{K}$ [20]) and lose mass at high rates ($10^{-5}\,\mathrm{M}_\odot/\mathrm{yr}$ [20]). WR stars typically begin their lives with masses above $30\,M_\odot$, shrinking to masses between $5\,M_\odot$ and $10\,M_\odot$ over the course of their evolution [19].

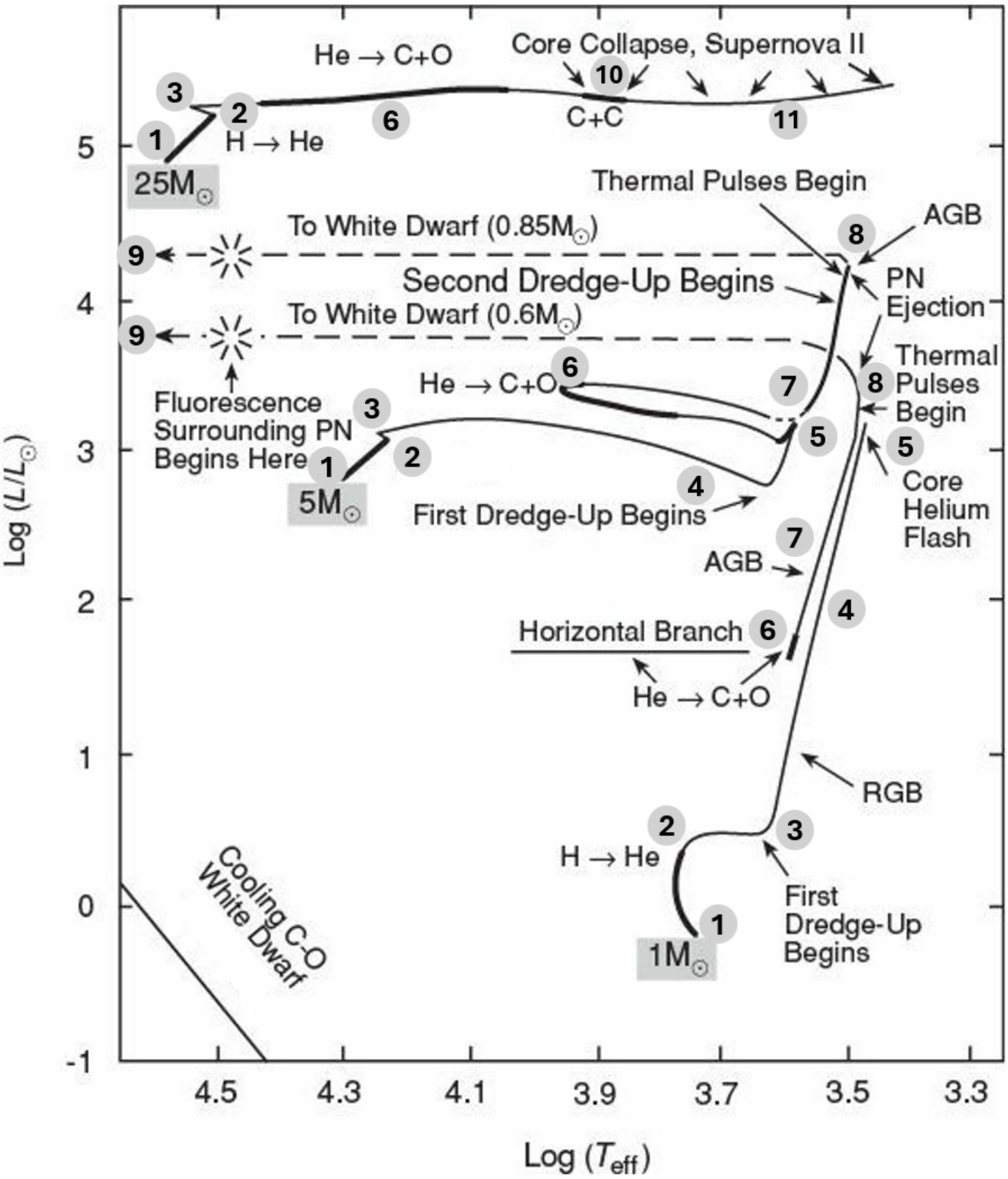

Fig. 2.1: Schematic HR diagram of the evolution of a $1\,M_{\odot}, 5\,M_{\odot}$ and $25\,M_{\odot}$ star. Thick segments denote long, nuclear-burning evolutionary phases. 1-2: Main Sequence (MS), 2: turn-off, 2-3: H shell-burning, 4-5: Red Giant Branch (RGB), 6: Horizontal Branch (HB), 7-8: Asymptotic Giant Branch (AGB), 8-9: Planetary Nebula (PN). 10: core collapse, 11: supernova type II. Adapted from [19].

A further notable class of massive stars are Luminous Blue Variable (LBV) stars. They are evolved post-main sequence stars and distinguish themselves by their variability, high mass-loss rates, temperatures and luminosities ($\sim 10^6\,\mathrm{L}_{\odot}$ [20]). These characteristics place them in the upper-left region of the HR diagram. LBV are so luminous that the *Eddington* luminosity limit [29] becomes relevant. This is the luminosity at which a star becomes unstable, since radiation pressure exceeds the star's self-gravity. Closely related to that is the *Humphreys–Davidson* limit [30], which represents the region in the upper-right of the HR diagram where stars become unstable because they approach the *Eddington* limit and begin to lose mass at very high rates.

2.2.3 Supernovae & stellar remnants

Supernovae (SNe) are incredibly luminous explosions with a brightness comparable to an entire galaxy. They are classified into Type I and Type II based on the presence or absence of hydrogen lines in their spectra. Types Ib, Ic and II SNe are associated with the core-collapse of massive, hydrogen-rich stars and are therefore not observed in older stellar populations. Type Ia SNe result from the collapse of a WR star that exceeds the *Chandrasekhar* mass limit. Since WR stars are present in both young and old populations, SNe Ia are observed in all types of galaxies.

The remnant left behind after a core collapse SN is either a Neutron Star (NS) or a Black Hole (BH), depending on the progenitor's mass. Neutron Stars consist of extremely dense matter supported by neutron degeneracy pressure. The upper mass limit of such objects is $2-3\,M_\odot$ [19]. Stars with masses $\gtrsim 60\,M_\odot$ leave behind cores that exceed this limit and collapse into BHs. The critical radius at which the escape velocity of an object becomes the speed of light, c, is given by the *Schwarzschild* radius [31]

$$R_\mathrm{S} = \frac{2GM}{c^2} \approx 3\frac{M}{M_\odot}\,\mathrm{km}\,, \tag{2.4}$$

such that any object compressed within this radius will form a BH.

2.3 Mass Loss from Stellar Winds

Mass loss is an important aspect of stellar evolution since it occurs in all evolutionary stages [19]. Mass can be lost from a star either from a sudden ejection of a mass shell, or a continuous flow, which is referred to as stellar wind. Mass-loss rates can vary over a wide range depending on the evolution stage and physical mechanism, however, the study of these mechanisms is not subject of this work (for a review see [28]).

In the standard model of stellar winds, winds are assumed to be stationary, homogeneous and spherically symmetric. In this case, the mass-loss rate $\dot{M}_\mathrm{wind}$, which represents the mass flux through a spherical shell of radius r, follows from the equation of continuity [28]:

$$\dot{M}_\mathrm{wind} = 4\pi r^2 \rho(r) v(r)\,, \tag{2.5}$$

where $\rho(r)$ is the density of the wind material and $v(r)$ its velocity. Developing models and empirical mass-loss prescriptions for different evolutionary phases is an active area of research [32][26][27][33].

Massive stars are far more affected by wind mass-loss than low- or intermediate-mass stars. Their winds are driven by the radiation field and therefore scale with luminosity and effective temperature. For example, a $15\,\mathrm{M}_\odot$ star loses mass on the MS at a rate of $1-2\cdot 10^{-8}\,\mathrm{M}_\odot/\mathrm{yr}$ [24], whereas a $40\,\mathrm{M}_\odot$ star typically loses mass at $\sim 10^{-6}\,\mathrm{M}_\odot/\mathrm{yr}$ [24]. Stars on the lower MS experience mass-loss rates that are too small to significantly affect their stellar mass, although even low-mass stars can develop strong winds during later evolution phases such as the AGB [19].

2.4 Binary Systems

The majority of massive stars are found in binary systems [34][18]. Binary systems are characterized by two stars (with masses M_1 and M_2) orbiting their common center of mass. In most binaries, the stars are separated far enough so that they do not influence each other's evolution. The stars then follow the evolutionary paths of single stars, differing only in the orbital dynamics of their point masses. Although stars in binary systems are born together, their masses can differ. This means that the stars may end up in different evolutionary stages at the same time. If the binary is close enough for the stars to interact, this can cause a variety of phenomena.

The two stars move in elliptical orbits characterized by the semi-major axis a and eccentricity e with their separation given by

$$d(\theta) = \frac{a(1-e^2)}{1+e\cos\theta}\,, \tag{2.6}$$

where θ is the angle between the distance vector and the major axis. Binaries that are close enough to interact typically have circular orbits ($e = 0$), which allows the individual masses to be determined observationally [19]. The orbital angular velocity ω follows from Kepler's third law:

$$\omega^2 = \frac{G(M_1+M_2)}{a^3}\,. \tag{2.7}$$

2.4.1 Gravitational potential & classification

A test mass placed within a binary system experiences the effective gravitational potential

$$\Phi = -G\left(\frac{M_1}{s_1} + \frac{M_2}{s_2}\right) - \frac{1}{2}\omega^2 r^2\,, \tag{2.8}$$

where G is the gravitational constant, r the distance of the test mass from the center of mass, and s_1, s_2 the distances of the test mass to each stars, respectively. The points at which the test mass experiences no net force are known as the *Lagranian* points L_i illustrated in Fig. 2.2. Close to each star, the equipotential surfaces are nearly spherical, but at larger distances they merge into a teardrop shape enclosing both stars. The inner Lagranian point L_1 and the teardrop-shaped regions it marks (so-called Roche lobes) play an essential role in interacting binary systems.

Binaries are classified according to how the stars fill these equipotential surfaces (see Fig. 2.3) [20][19]. Stars that have a separation that is much larger than their radii are called detached binaries. In this case, the stars do not interact with each other and evolve independently. Once one of the stars fills its Roche lobe, material can escape through the inner Lagranian point and can be accreted by the other star. This system is called semi-detached binary. The star losing mass is called the secondary star, which typically has the smaller mass M_2. The companion star that is accreting material from the secondary star is called the primary star, usually having the greater mass M_1. If both stars expand beyond their Roche lobe, they will share a common envelope and the system is referred to as a contact binary.

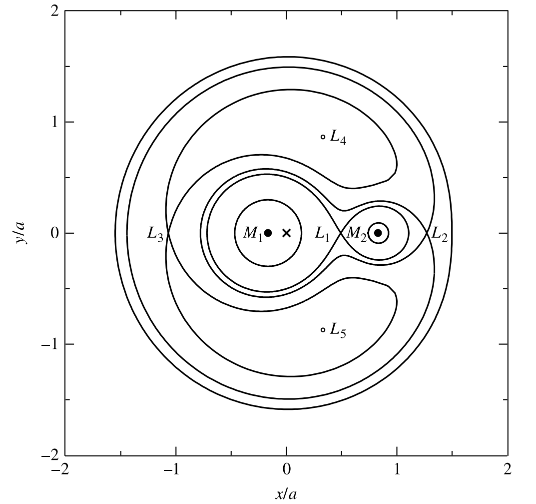

Fig. 2.2: Equipotential contours of a binary system with stars of masses $M_1 = 0.85\,\mathrm{M}_\odot$ and $M_2 = 0.17\,\mathrm{M}_\odot$, and a separation of $a = 0.718\,\mathrm{R}_\odot$. The x denotes the center of mass [20].

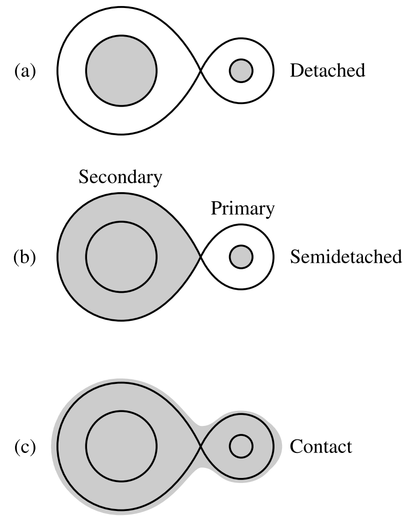

Fig. 2.3: Classification of close binary systems [20].

2.4.2 The evolution of interacting binaries

The evolution of an interacting binary system results from the interplay between the stellar evolution of its components and their interaction. It depends on the stars' initial masses and their separation.

Semi-detached binaries lead to a range of mass transfer phenomena, which can be either conservative or non-conservative. In conservative mass loss, the accreting star retains all transferred mass, and both the total mass and orbital angular momentum of the binary system are conserved. In non-conservative mass transfer, a fraction of the transferred mass is lost from the binary entirely. Two different scenarios can occur: If the more massive star fills its Roche lobe first, it loses mass to its companion until the mass ratio reverses. If instead the less massive star fills its Roche lobe first, the result is typically a stable accretion phase, which can result in eruptive phenomena such as Novae in so-called Cataclysmic Variables [19]. The rate of mass transfer $\dot{M}_\mathrm{t}$ can be estimated as

$$\dot{M}_\mathrm{t} = \rho v A\,, \tag{2.9}$$

where ρ is the density of the stellar material, v its velocity, and A the area through which it escapes. The star that loses mass is referred to as the *donor*, and the star that gains mass is called *accretor*. In most cases, both stars first evolve independently of each other until one expands to fill its Roche lobe and begins transferring mass to its companion. The binary may go through common-envelope phases, or even evolve into a Double Compact Object (DCO) consisting of two Neutron Stars, Black Holes, or one of each. Those might merge entirely, or become disrupted due to a SN event.

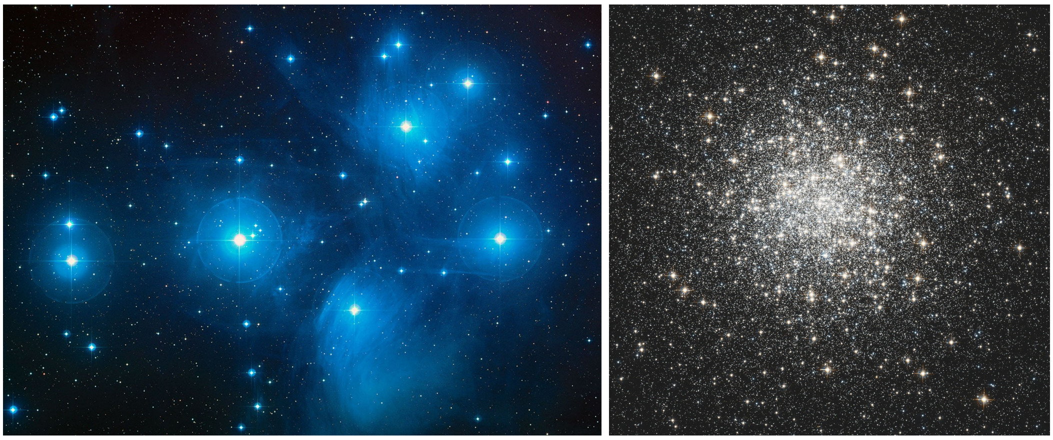

(a) **(b)**

Fig. 2.4: (a) The Pleiades, a young ($\sim$ 100 Myr) open cluster in Taurus $\sim$ 130 pc away. Captured by the Schmidt telescope at the Palomar Observatory in California *Credit: NASA, ESA, and AURA/Caltech.* (b) The core of Messier 3, a globular cluster ($\sim$ 11 400 Myr) at $\sim$ 10 000 pc. Constructed using Hubble observations in visible and infrared light. *Credit: NASA, ESA, STScI and A. Sarajedini (University of Florida).*

2.5 Stellar Clusters

Stars often move together through the galaxy and are gravitationally bound to one another [9]. Such "stellar over-densities" are referred to as stellar clusters. In many galaxies, stellar clusters make up a large fraction of the total stellar population, sometimes containing tens or even hundreds of thousands of stars. Therefore, stellar clusters have a significant impact on the surrounding interstellar medium and the evolution of the galaxy [19][20]. Cluster members are assumed to have formed at approximately the same time from a common gas cloud and therefore have an identical initial composition. Neglecting the effects of rotation, magnetic fields and binary interactions, their evolution depends predominantly on their initial masses. Stars within a cluster experience stronger gravitational attraction to each other than to non-members. Since the separations between cluster members are small compared to their distance from an observer, all member stars can be treated as having approximately the same distance.

2.5.1 Globular vs. open stellar clusters

Stellar clusters can be divided into two categories, globular clusters and open clusters. Globular clusters are spherical, dense and very massive, typically containing $\sim 10^5$ stars [20]. Such clusters formed when the galaxy was still very young and therefore consist of old stellar populations ($\sim$ Gyr). Globular clusters are found at high galactic altitudes, orbiting the halo of the galaxy. Open clusters are significantly younger and less massive and are mainly located in the galactic disc. They usually contain a few hundred stars. The member stars of open clusters often seem to have a random arrangement, giving the cluster an irregular shape. Open clusters trace the young population of stars and thus have ages in the order of $\sim$ 100 Myr [9]. Fig. 2.4 shows two examples of stellar clusters: (a) the Pleiades, a young open cluster, and (b) Messier 3, a globular cluster.

Distinguishing open and globular clusters in observations requires certain selection criteria. Hunt & Reffert [35], for example, identify open clusters from *Gaia* data the following way. A potential open cluster has to be a clear over-density of at least 10 stars of approximately the same age and chemical composition. In addition, the cluster candidate has to be compact enough by having a median radius smaller than 15 pc. The stars have to move coherently together by having an internal velocity dispersion below 5 km/s. Hunt & Reffert [35] further distinguish between bound and unbound open clusters. Bound clusters have a self-gravity that can keep the members confined, while unbound clusters have a common age and motion but are not gravitationally bound.

2.5.2 HR diagrams of stellar clusters

The HR diagram of a stellar cluster gives insights into a range of cluster properties [20]. For instance, if the cluster's distance is known, the distance modulus can be determined via main-sequence fitting, in which the cluster's observed MS in apparent magnitude is matched to a calibrated MS in absolute magnitude. Cluster HR diagrams often display the colour index $(B - V)$ instead of the effective temperature, since it is easier to measure. The resulting diagram is referred to as colour-magnitude diagram, as shown in Fig. 2.5.

The curve that results from plotting the position of every member star at the cluster's current age is called *isochrone*. The number of stars at each position on the isochrone depends on the number of stars in each mass range and the rate at which stars evolve through each phase. Since more massive stars evolve faster, they reach and leave the MS sooner than less massive stars. The point at which stars are currently leaving the MS *(turn-off point)* therefore marks the most massive stars that still remain on the MS. In a young cluster, where only the most massive stars have evolved past the MS, the turn-off point lies higher on the MS. As the cluster ages, this point shifts to a lower position in the diagram. This provides a way to estimate the age of stellar clusters.

A characteristic feature of the colour-magnitude diagram of young clusters is the so-called Hertzsprung Gap (HG). It describes the absence of stars between the end of the MS and the RGB, indicating that stars evolve through this phase very rapidly. The HG appears only in young clusters, since stars in old stellar clusters evolve more gradually towards the giant branch [20].

2.5.3 Initial Mass Function & binary fraction

The collapse of an interstellar cloud produces stars across a wide range of masses. The number distribution of stellar masses at their formation is described by the stellar initial mass function $\xi(M)$ (IMF). The classical formulation of Salpeter [36] treats the IMF as an invariant probability density function such that the number of stars dN formed in a mass interval $(M, M + dM)$ is

$$dN = \xi(M)dM \,. \tag{2.10}$$

The Salpeter IMF follows as a single power-law

$$\xi(M) \propto M^{-2.35} \,. \tag{2.11}$$

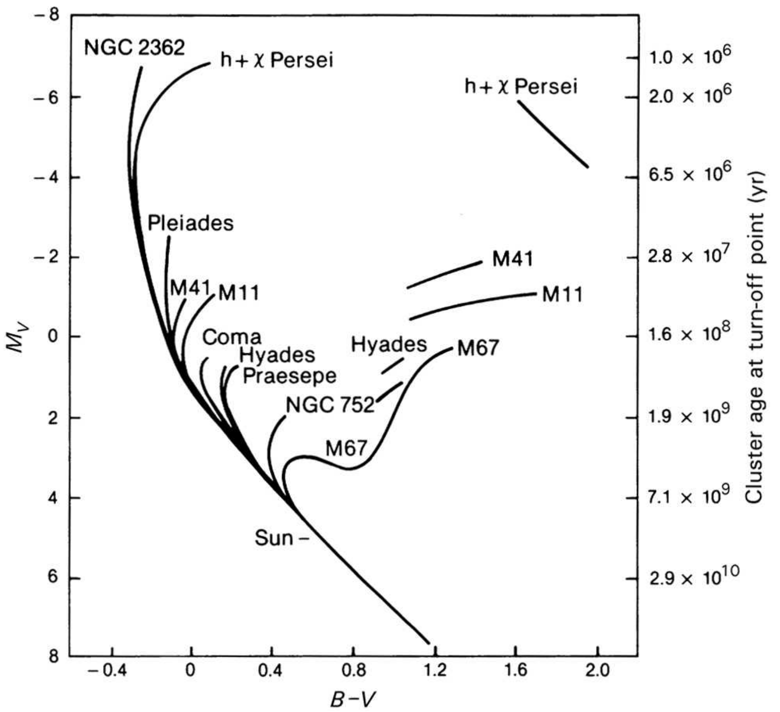

Fig. 2.5: Schematic colour-magnitude diagram for a set of Galactic clusters. Left-hand vertical axis: absolute visual magnitude M_V, right-hand vertical axis: age of the cluster based on the turn-off point. Horizontal axis: colour-index $B - V$ [20].

The IMF implies that the number of formed stars decreases with increasing mass, i.e. low-mass stars are far more abundant in stellar clusters than high-mass stars. Despite their scarcity, they have an important influence on cluster evolution. They are far more luminous, have stronger stellar winds and serve as progenitors of SNe. Massive stars therefore shape the evolution of stellar populations in a far more significant way than what their number alone would suggest [20].

While the Salpeter IMF is a good description for intermediate- and high-mass stars, it has an uncertainty at the low-mass end. Also, observations suggest that the IMF depends on environmental factors such as the local conditions of the star forming region [23]. Weidner & Kroupa [37] introduced a multiple-part power law IMF, based on observations of nearby stellar populations. Their model keeps the slope from Salpeter [36] for intermediate- and high-mass stars, but has modified exponents below $1\,\mathrm{M}_\odot$:

$$\xi(M) = k \cdot \begin{cases} \left(\dfrac{M/\mathrm{M}_\odot}{0.08}\right)^{-0.30}, & 0.01 \leq M/\mathrm{M}_\odot \leq 0.08, \\ \left(\dfrac{M/\mathrm{M}_\odot}{0.08}\right)^{-1.30}, & 0.08 \leq M/\mathrm{M}_\odot \leq 0.50, \\ \left(\dfrac{0.50}{0.08}\right)^{-1.30} \left(\dfrac{M/\mathrm{M}_\odot}{0.50}\right)^{-2.30}, & 0.50 \leq M/\mathrm{M}_\odot \leq 1.00, \\ \left(\dfrac{0.50}{0.08}\right)^{-1.30} \left(\dfrac{1.00}{0.50}\right)^{-2.30} \left(\dfrac{M/\mathrm{M}_\odot}{1.00}\right)^{-2.35}, & 1.00 \leq M/\mathrm{M}_\odot \leq M_{\mathrm{max}}. \end{cases} \tag{2.12}$$

Here k denotes the normalization factor and M is given in solar masses. A comparison

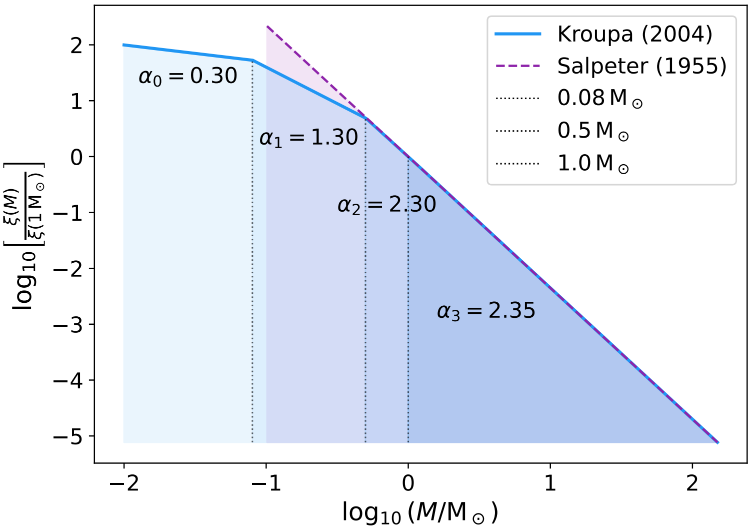

Fig. 2.6: Double-logarithmic plot of the Weidner & Kroupa [37] and Salpeter [36] IMFs, normalized to $\xi(1\,\mathrm{M}_\odot) = 1$. The slopes of the multiple-part Kroupa IMF are $\alpha_0 = 0.30$, $\alpha_0 = 1.30$, $\alpha_0 = 2.30$, $\alpha_0 = 2.35$. Characteristic break masses are indicated by vertical lines $(0.08\,\mathrm{M}_\odot,\ 0.5\,\mathrm{M}_\odot,\ 1.0\,\mathrm{M}_\odot)$. The slope of the Salpeter IMF is 2.35.

of the Kroupa and Salpeter IMF slopes, both normalized to $\xi(1\,\mathrm{M}_\odot) = 1$, is shown in Fig. 2.6. From the IMF, the number of stars N^* between a theoretical minimum mass M^*_{min} and maximum mass M^*_{max} follows as [37]

$$N^* = \int_{M^*_{\mathrm{min}}}^{M^*_{\mathrm{max}}} \xi(M) dM \tag{2.13}$$

and the total mass of the cluster is given by

$$M_c = \int_{M_{\mathrm{min}}}^{M_{\mathrm{max}}} M\xi(M) dM\,, \tag{2.14}$$

where M_{max} and M_{min} denote the smallest and largest stellar masses in the cluster.

The fraction of stars found in binary systems is described by the binary fraction f of a cluster. It depends on the population of stars the cluster contains and is a function of stellar mass. Typically, the binary fraction is higher for massive stars and lower for less massive stars [23]. Overall, binary fractions are estimated at 50–70%, and in some cases even as high as 90% [38][13]. Binaries can occur in various separations, orbital periods and mass ratio distributions. Some studies find that in some clusters component masses seem to be drawn independently from the IMF, while others suggest that binaries with short orbital periods have nearly equal component masses [13]. In young massive clusters, binaries can significantly influence the dynamical evolution and the mass distribution of the cluster. The binary fraction is generally assumed to be uniform throughout the cluster at birth and increases toward the center as the cluster ages [38].

3 Introduction to COMPAS

COMPAS, short for "Compact Object Mergers: Population Astrophysics and Statistics", is a rapid binary population synthesis code developed by *J. Riley et al.*. It has been used to study different astrophysical phenomena such as compact objects, mergers and gravitational waves [12].

3.1 Code Architecture

COMPAS uses a set of models and methods to evolve isolated stars or binaries from ZAMS to their final states. The core BPS code is written in C++ and combines prescriptions for single-star evolution (SSE) and binary-star evolution (BSE). Stellar attributes such as luminosity, radius and temperature are provided by the SSE code, which covers all evolutionary stages of single stars. The BSE code contains additional algorithms that capture the interactions specific to binaries. The evolution of a binary system is stopped if one of the following conditions is met: (a) a DCO has formed, (b) the binary is disrupted, (c) the component stars merge, or (d) the maximum evolution time or maximum number of evolutionary steps is exceeded. Both the maximum evolution time and step count can be specified by the user, or otherwise set to $t = 14\,000\,\mathrm{Myr}$ and 99 999 time steps [12].

The duration of a time step is estimated by the description of Hurley et al. [39], depending on the star's evolutionary stage. COMPAS then evaluates the stellar and binary properties during that time step and checks whether the time step has caused excessive change (mass loss $> 1\%$ or radial change $> 10\%$). If so, the time step is reduced and the parameters re-evaluated. The adaptive time-stepping method ensures that a star does not skip over multiple evolutionary phases within a single step and transition between stellar types are captured accurately. A consequence of this approach, however, is that each star or binary system has its own individual timeline, with stellar parameters evaluated at time steps specific to it. This must be accounted for when post-processing simulations of cluster-like populations, which require a common timeline for all systems.

COMPAS can be run in several different ways, for example, directly from the command line, by Python scripts, or by using a grid files that specify initial parameters to each binary system separately.

3.2 Single Star & Binary Evolution

3.2.1 Evolutionary models

Radii and luminosities at ZAMS are derived from the initial mass and metallicity by using the analytic formulae of Tout et al. [40]. For stellar evolution, COMPAS uses the analytical fits of Hurley et al. [39] to the models of Pols et al. [41], which express stellar luminosities and radii as functions of age. From the moment a star is created, COMPAS integrates its physical attributes as functions of mass, metallicity and age. Since the Pols et al. [41] models extend only to ZAMS masses of $50\,M_\odot$, COMPAS extrapolates them up to $150\,M_\odot$.

The SSE code captures the evolutionary stages of single stars described in chapter 2.2.2. Each stars is assigned a stellar type (0-15) according to the classification scheme of Hurley et al. [39]. The additional type 19 serves as placeholder if the stellar type has not been assigned yet. An overview of the stellar types and their abbreviations is given in Tab. 3.1.

Stellar phase	**Abbreviation**	**Number**
Main sequence, $M < 0.7\,M_\odot$	MS	0
Main sequence, $M > 0.7\,M_\odot$	MS	1
Hertzsprung gap	HG	2
First giant branch	FGB	3
Core helium burning	CHeB	4
Early asymptotic giant branch	EAGB	5
Thermally pulsing asymptotic giant branch	TPAGB	6
Helium main sequence	HeMS	7
Helium Hertzsprung gap	HeHG	8
Helium giant branch	HeGB	9
Helium white dwarf	HeWD	10
Carbon–oxygen white dwarf	COWD	11
Oxygen–Neon white dwarf	ONeWD	12
Neutron star	NS	13
Black hole	BH	14
Massless remnant	MR	15
Chemically homogeneous evolution	CHE	16
...	NONE	19

Tab. 3.1: Stellar phases and abbreviations used in COMPAS [12]

The interaction of stars in binary systems is modelled through different prescriptions for mass transfer, common-envelope evolution and gravitational-wave emission. Binary interactions are triggered once a star fills its Roche lobe. Any resulting changes to stellar parameters are then transferred back to the SSE code.

3.2.2 Wind mass loss & stellar remnants

COMPAS uses three analytical prescriptions to model stellar wind mass loss, Hurley et al. [39], Belczynski et al. [42] and Merritt et al. [33] (in prep.). Hurley et al. [39] determines the mass-loss rate from the dominant mechanism at which the star loses mass during each evolutionary stage. The model of Belczynski et al. [42] combines separate prescriptions for different stellar classes, including WR and LBV stars. The Merritt et al. [33] suite updates the treatment of winds from massive stars ($> 100\,\mathrm{M}_\odot$) and WR stars. Regardless of the chosen prescription, COMPAS caps the maximum allowed mass-loss rate at $0.1\,\mathrm{M}_\odot\,\mathrm{yr}^{-1}$. When mass is lost from a binary system, COMPAS assumes the material is leaving spherically symmetrically as described in the standard model in chapter 2.3. Wind accretion, wind Roche-lobe overflow, or interactions between the stellar wind and the companion star are not being modelled.

COMPAS evolves low- and intermediate-mass stars ($\lesssim 8\,\mathrm{M}_\odot$) into WDs, adopting the *Chandrasekhar* mass ($1.4\,\mathrm{M}_\odot$) as the mass limit. Stars with masses $\gtrsim 8\,\mathrm{M}_\odot$ evolve into neutron stars or black holes via SN explosions. The remnant mass depends on the specific SN type, whereas the maximum allowed NS mass is set to $2.5\,\mathrm{M}_\odot$ [12].

As an illustration of mass loss from winds and SNe in COMPAS, Fig. 3.1 shows the evolution of a simulated massive star. It was drawn from a test population of 100 binary systems run in default BSE mode. The star has a ZAMS mass of $18.8\,\mathrm{M}_\odot$ and undergoes several mass-loss phases before its evolution ends at $6.52\,\mathrm{M}_\odot$. On the MS (stellar type 1), the star loses mass gradually at a mean rate of $7.14 \cdot 10^{-8}\mathrm{M}_\odot/\mathrm{yr}$. Its luminosity rises and temperature falls, as expected from the evolution of massive stars. At an age of $\sim 9.86\,\mathrm{Myr}$, the star transitions to stellar type 4, marking the onset of core helium burning. At this stage the star's envelope becomes more loosely

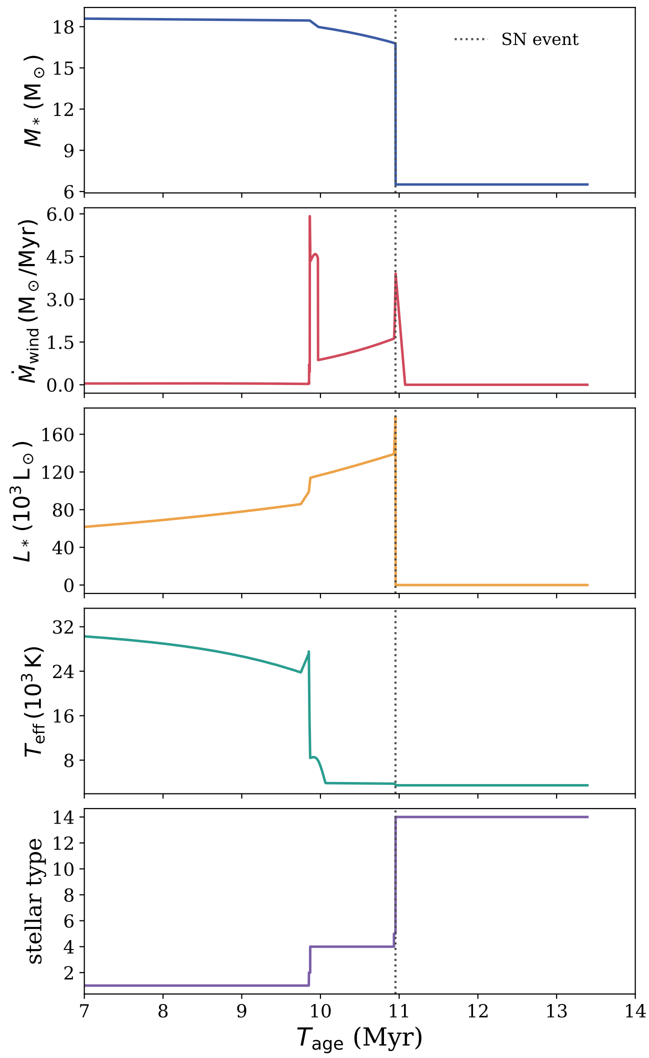

Fig. 3.1: Evolution of stellar mass $M_\star$, wind mass-loss $\dot{M}_{\mathrm{wind}}$, luminosity $L_\star$, effective temperature T_{eff} and stellar type for a massive star selected from a COMPAS test run of 100 binaries in BSE default mode. Stellar types are enumerated according to Tab. 3.1. The star undergoes a SN event at $\sim 11.0\,\mathrm{Myr}$ (dotted line), forming a BH.

bound, leading to stronger wind mass-loss with a peak rate of $5.92 \cdot 10^{-6} \mathrm{M}_{\odot}/\mathrm{yr}$. The luminosity continues to increase while the temperature drops, indicating that the star evolves into a red supergiant. The final evolutionary phases proceed faster compared to the MS lifetime. The star reaches the Early Asymptotic Giant Branch (EAGB) at 10.94 Myr and undergoes a SN explosion shortly afterward (10.95 Myr). It leaves behind a BH remnant with a mass of $6.52\,\mathrm{M}_{\odot}$. In total, the star loses $\sim 65\%$ of its initial mass, with 55% of that loss occurring during the SN event. Up to the first major mass-loss episode at ~ 10 Myr, the dominant wind mechanism is classified as the one of an OB main-sequence star (a hot, massive stars of spectral types O or early B). Later it transitions to the wind mechanism characteristic to a red supergiant. Overall, the behaviour shown in Fig. 3.1 is consistent with the expected evolutionary path of a massive star described in chapter 2.2.2.

3.3 Evolving Cluster-like Populations

At the start of a simulation, each star and binary system is assigned its initial ZAMS parameters like mass, metallicity, separation and eccentricity. Those can either be specified by the user directly, or sampled from chosen distributions. The population evolved by COMPAS represents a sampled subset from which conclusions about the actual population can be drawn. Also, COMPAS assumes that each initial parameter can be sampled independently of the others. The following discussion focuses on evolving populations in BSE mode, which is the relevant mode for the cluster simulations presented in later chapters. Unless specified by the user, COMPAS draws the primary masses $M_{1,i}$ from a Kroupa [43] IMF in the default mass range $[5, 150]\,\mathrm{M}_{\odot}$. Secondary masses $M_{2,i}$, are determined via the mass ratio

$$q_i = \frac{M_{2,i}}{M_{1,i}} \tag{3.1}$$

with q_i drawn uniformly from the range of $[0.01, 1]$ by default. The initial semi-major axes a_i are sampled from a log-uniform distribution $p(a_i) \propto 1/a_i$, if not otherwise defined, over the default range $[0.01, 1000]$ AU. The sampling of semi-major axes is independent of stellar masses. All binaries are assumed to be circular at birth ($e_i = 0$) and all stars are assumed to be non-rotating initially. A complete description of the default parameters can be found in Table 1 of the COMPAS method paper [12] or in the online documentation[2]. The HR diagram of selected stars from a population simulated in BSE default mode, evolved to ~ 14 Myr, is shown in Fig. 3.2.

To simulate populations that are consistent with stellar clusters, several parameters must be adjusted from the default settings. To specify a binary fraction for each cluster, a subset of the simulated systems must be evolved as effectively single stars. This can be achieved by assigning such systems a very large semi-major axis so that any possible interaction during the evolution time is prevented. Therefore, for each cluster a grid file was generated, which specifies semi-major axes for each star. Systems intended to behave effectively single are assigned $a = 10^5$ AU or larger, while the semi-major axes of genuine binaries are sampled from a log-uniform distribution in $[0.01, 30]$ AU. The resulting ZAMS semi-major axis distribution for a population of $\sim 11\,600$ stars with a

[2] `https://compas.science/docs/`

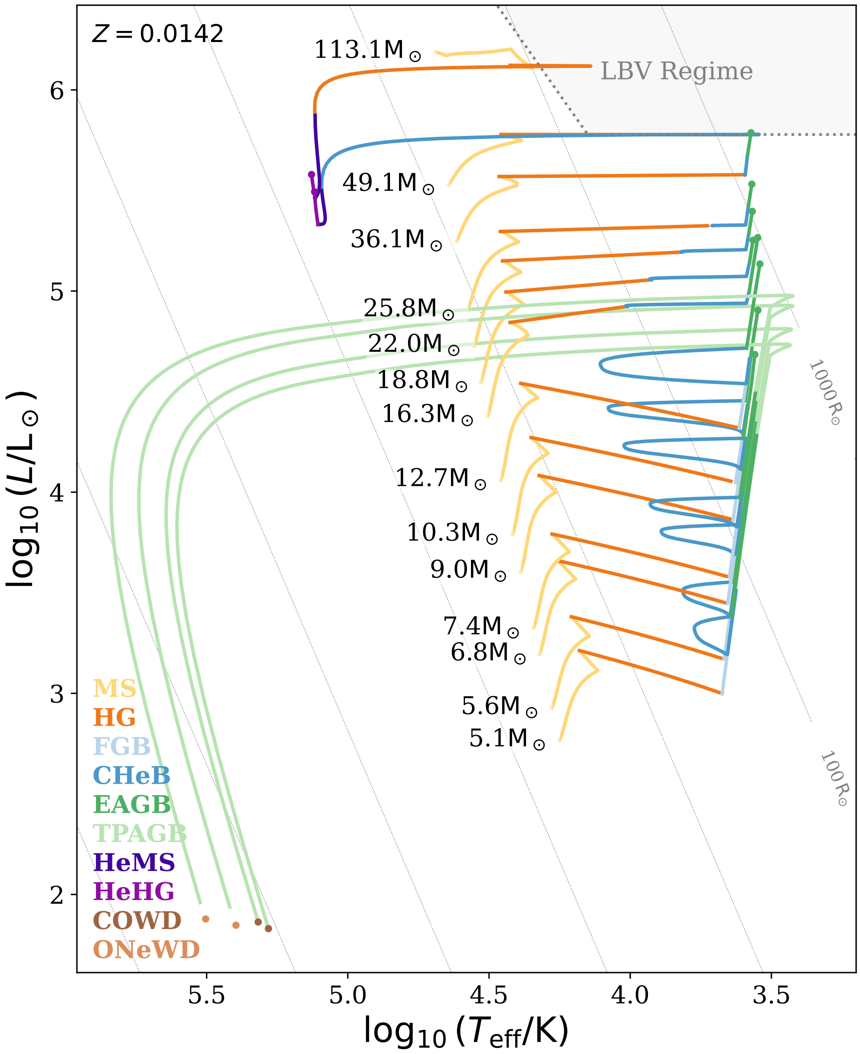

Fig. 3.2: Evolutionary tracks of selected stars from a population simulated in default BSE mode at solar metallicity ($Z = 0.0142$). The grey region in the upper right marks the *Humphreys-Davidson* limit. Lines of constant radii are shown as grey diagonals. The HR diagram was plotted using Python scripts provided by [12].

binary fraction of 30% is shown in Fig. 3.3a. Primary star masses are drawn from the IMF given in Eq. 2.12 in the mass range of $[0.08, 150]\,\mathrm{M}_\odot$ according to the theoretical model described in Section 2.1. Secondary masses are computed as $M_{2,i} = q_i M_{1,i}$ with the mass ratio sampled as in default mode, but with a fixed minimum secondary mass of $0.1\,\mathrm{M}_\odot$. The resulting initial mass distribution for the same test cluster as before is shown in Fig. 3.3b.

All stars are “born” simultaneously at the begin of a simulation and start their evolution at ZAMS at the same time. This is consistent with the assumption that stars in stellar clusters approximately form at the same time (see chapter 2.5). The cluster can then be evolved up to a desired age by setting that age as the maximum evolution time of the run. Metallicity is specified as a global parameter shared by all stars in the cluster.

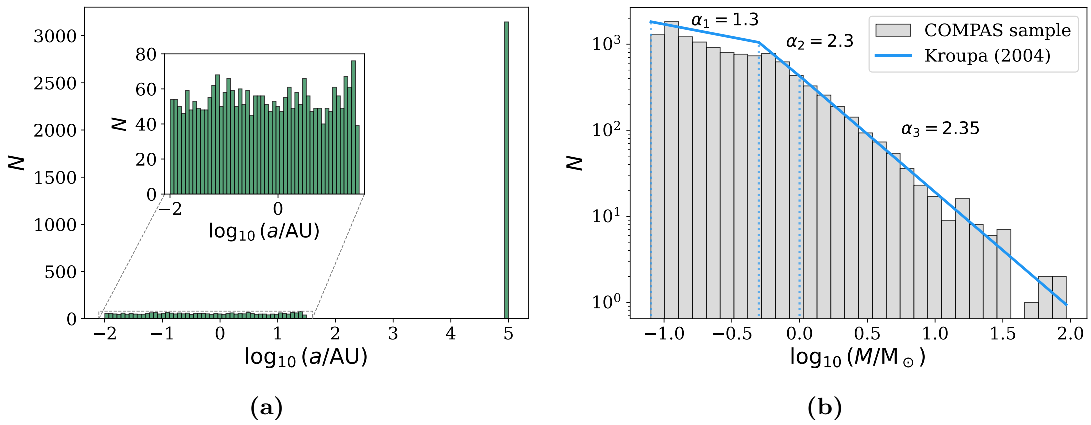

Fig. 3.3: (a) Initial semi-major axis distribution of a population including $\sim$ 5800 stars with a binary fraction of 30%. Binaries supposed to evolve as two single stars are assigned $a = 10^5$ AU, for functional binaries semi-major axes are sampled from a log-uniform distribution in $[0.01, 30]$ AU. (b) Initial mass distribution of the same test cluster compared to the theoretical IMF as in Eq. 2.12. $M_{1,i} \in [0.08, 150]\,\mathrm{M}_\odot$ and $M_{2,i} = q_i M_{1,i}$ with a minimum secondary mass of $0.1\,\mathrm{M}_\odot$.

This agrees with the assumption that cluster members have formed from the same gas cloud and thus have similar chemical compositions.

The primary interest of this study is to estimate cluster parameters such as mass, wind mass-loss, and SN counts from the simulated populations. Since COMPAS evolves each binary along its own timeline (see chapter 3.1) cluster members do not have the same set of time steps. To evaluate cluster quantities at a given cluster age, a global timeline is therefore constructed from the individual time steps of all binaries. The cluster mass at a given time t is then obtained by interpolating each star's mass onto this global timeline and summing over all systems:

$$M_c(t) = \sum_i [M_{1,i}(t) + M_{2,i}(t)]\,. \tag{3.2}$$

The same procedure is used to determine the cluster wind mass-loss rate:

$$\dot{M}_{\mathrm{wind}}(t) = \sum_i [\dot{M}_{1,i}(t) + \dot{M}_{2,i}(t)]\,, \tag{3.3}$$

where $\dot{M}_1$ and $\dot{M}_2$ denote the wind mass-loss rates of the primary and secondary stars, respectively, and i runs over all simulated systems.

Discrete quantities such as the instantaneous wind mass-loss M_{wind}, or events like SNe or mass transfer episodes are evaluated directly at each time step without interpolation. M_{wind} and M_{MT} thus represents the mass lost from stellar winds or mass transfer in single time steps. SN mass-loss is computed as the difference between the stellar mass immediately before the collapse and the mass of the compact remnant. The total mass lost in SN events M_{SN} is then obtained by summing over all SN events:

$$M_{\mathrm{SN}} = \sum_i [M_{\mathrm{preSN,i}} - M_{\mathrm{remnant,i}}]\,. \tag{3.4}$$

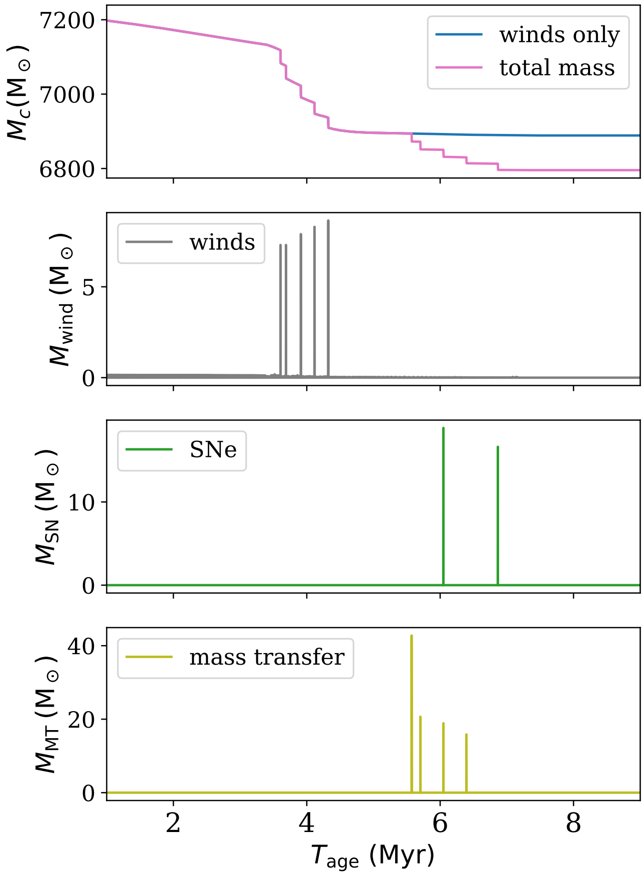

Fig. 3.4: Mass evolution of a test cluster containing $\sim 11\,600$ stars (binary fraction set to 30%, primary masses sampled from Weidner & Kroupa [37] IMF) on a global timeline. Total cluster values are obtained by summing over all member stars at each cluster age.

Fig. 3.4 shows the evolution of a population consistent with a stellar cluster of $\sim 11\,600$ stars in the interval of $1-9\,\mathrm{Myr}$. The phases of cluster mass-loss align with the spikes of mass loss from the different processes (wind mass-loss, SN mass-loss and mass transfer). Until an age of $\sim$ 5Myr the population loses mass solely from winds with mass-loss peaks marking post-main sequence phases of massive stars. As the population ages, mass transfer spikes appear, marking the interaction between binary members. The population experiences two SN events, one of them accompanied by excessive mass transfer, suggesting that the SN is the result of an interacting binary system.

4 Simulating Young Galactic Open Clusters

4.1 *Gaia* Mission & Stellar Cluster Catalogues

Gaia is a space mission of the European Space Agency (ESA) that has been collecting data of the Milky Way between 2014 and 2025. *Gaia*'s observations contain astrometric, photometric and spectroscopic data on about two billion stars and other objects. They provide a very precise survey of the Galaxy, advancing our understanding of its structure and evolution [8]. The second *Gaia* data release (DR2) was published in 2018 from which about 2000 stellar clusters could be identified [10]. Four years later, *Gaia*'s third data release (DR3) added another 12 months of observations with improvements in data precision. These advances allowed distant clusters to be detected, increasing the number of identified clusters to more than ~ 6000 [11]. The following paragraphs introduce three catalogues of cluster parameters (Hunt & Reffert [11], Almeida et al. [44] and Celli et al. [45]) that were used as input and references for the simulations in this work.

Hunt & Reffert [11] created a homogeneous stellar cluster catalogue containing 7167 clusters using *Gaia* DR3 data. They performed a blind, all-sky search for open clusters down to a magnitude of $G \sim 20$ and identified 2387 new cluster candidates. In a following paper [35] they obtain the cluster masses of a subset of bound clusters by integrating a fitted Kroupa IMF. They also account for unresolved binaries and other corrections of the data incompleteness. Their computation shows that the correction for unresolved binaries alone can increase the mass estimate by $10\% - 20\%$.

Almeida et al. [44] introduced a new method for determining open cluster masses based on the masses of individual member stars. They start by generating synthetic clusters from *Gaia*'s early data release 3 (eDR3) and then compare them to observed clusters via a Monte Carlo method. That way, they estimate individual star masses and their uncertainties. The total cluster mass is then obtained from the member star masses. Additionally, they include the mass of unseen low-mass stars and the mass contained in stellar remnants and unresolved binaries. Beyond cluster masses, their method also determines the ages, distances and binary fractions for 773 open clusters.

Celli et al. [45] developed a method to estimate the masses of young open clusters from *Gaia* DR2. They start from the number and magnitude of observed stars and obtain the IMF normalization factor by inverting the IMF integral (Eq. 2.13) evaluated at the observed mass range $[M^{\star}_{\rm min}, M^{\star}_{\rm max}]$. The total cluster mass is then obtained by extending the integration of the IMF to the full theoretical mass range $[0.08\,\mathrm{M}_{\odot}, M_{\rm max}]$. $M_{\rm max}$ is constrained by both the cluster age and the parent cluster mass. They determine the masses, mass-loss rates and wind luminosities of 387 young clusters. The authors emphasize that their mass estimates should be understood as lower limits, since binary stars, unresolved members, and incomplete member identification are not considered.

4.1.1 Normalising the IMF

The number of stars that should be simulated for each cluster can be determined from the normalization of the IMF (Eq. 2.12). For *Gaia* DR2, normalization values are taken directly from Celli et al. [45]. The total number of stars per cluster, N_i^*, then follows by integrating the IMF over the theoretical mass range $M^*_{\rm min} = 0.08\,\mathrm{M}_{\odot}$ to $M^*_{\rm max} = 150\,\mathrm{M}_{\odot}$ as in Eq. 2.13.

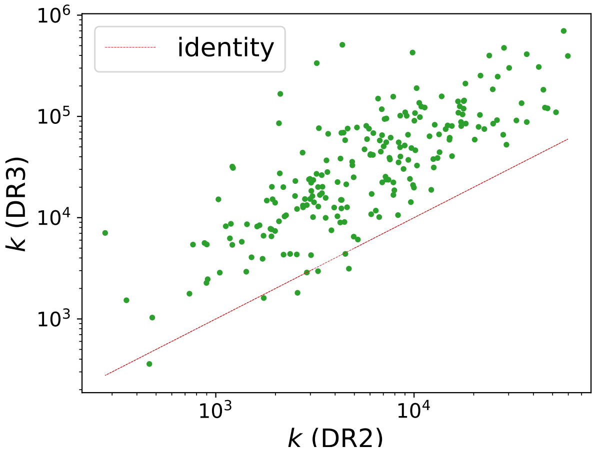

Fig. 4.1: Comparing normalization factors from *Gaia* DR2 and DR3. k-values derived from *Gaia* DR2 are taken from Celli et al. [45], k-values from *Gaia* DR3 are determined by using stellar and cluster masses from Hunt & Reffert [35]. The identity line marks where both k-value sets would be equal to each other.

For *Gaia* DR3, k-values are determined from the Hunt & Reffert [35] catalogue. Rearranging Eq. 2.14 yields the normalization factor as

$$k_{\mathrm{DR3}} = \frac{M_c^{\mathrm{H}}}{\int_{M_{\mathrm{med}}^H}^{M_{\mathrm{max}}^H} \xi(M) M dM} \,. \tag{4.1}$$

M_c^{H} is the respective total cluster mass from Hunt & Reffert [35] and M_{max}^H the mass of the cluster's most massive member. Because faint, low-mass stars are difficult to detect, observational data is incomplete at the low-mass end. Using the minimum observed member mass as the lower integration bound in Eq. 4.1 would therefore overestimate the true observed cluster mass (and consequently underestimate the normalization factor). To avoid this, the median member mass M_{med}^H is instead used as the lower integration bound, restricting the integral to the mass range where the catalogue is reasonably complete. Once the k-values are obtained we can use Eq. 2.13, again integrated over $[0.08, 150]\,\mathrm{M}_\odot$, to get the total number of stars per cluster[3]. For the simulation, a sample of young ($< 30\,\mathrm{Myr}$) clusters from Hunt & Reffert [35] was selected.

A comparison of the DR2 and DR3 k-values is shown in Fig. 4.1. The DR3 values show a systematic offset from the identity line in log-log space. This suggests that the higher sensitivity of *Gaia* DR3 captures not only more low-mass stars, but generally a larger number of stars across all mass ranges. Both methods predict a total number of stars per cluster that is larger than the observed one, as can be seen from the histogram shifts in Fig. 4.2.

Simulating the full predicted number of stars for each cluster would require large computing time and data storage. Therefore, only 20% of the predicted stellar population

[3] The obtained normalization factors and stellar counts per cluster are provided in `https://github.com/annarose-22/modeling-stellar-clusters`, as well as in Tab. A.4, A.5 and A.6 for the ten most massive clusters in each COMPAS run.

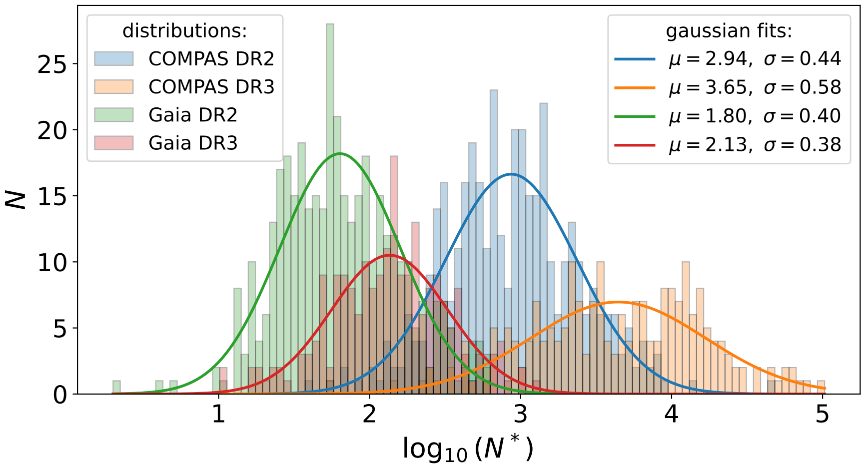

Fig. 4.2: Comparing number of stars per cluster N^* calculated from *Gaia* DR2 (blue), DR3 (orange) and stellar counts from observational data by *Gaia* DR2 (green) and DR3 (red). The former data was taken from [10], the latter from [35]. For DR2, 387 clusters were taken into account, for DR2, 215 clusters.

per cluster will be simulated. This fraction is sufficient to obtain a representative sample of the cluster. During post-processing, all derived cluster quantities are then scaled up to match the full predicted stellar population.

4.1.2 Initial parameters of COMPAS runs

In the course of this thesis three major COMPAS simulations were performed. The first (DR2(1)-run) contained the 387 young open clusters selected by Celli et al. [45], with primary masses sampled from the COMPAS default IMF in the mass range $[5, 150]\,\mathrm{M}_\odot$. Secondary masses were determined via a mass ratio $q \in [0.01, 1]$, such that the effective lower mass limit is $0.05\,\mathrm{M}_\odot$. Metallicities were taken from Kharchenko et al. [46] and set to solar metallicity (0.0142), where no metallicity values was provided. The binary fraction was set to $f = 0$, i.e. all systems were assigned a separation of 10^{20} AU.

The second simulation (DR2(2)-run) used the same cluster sample, but with a wider IMF range ($[0.08, 150]\,\mathrm{M}_\odot$) following Weidner & Kroupa [37]. The minimum mass of secondary stars was set to $0.08\,\mathrm{M}_\odot$ and metallicities and binary fractions were taken from Almeida et al. [44] (set to $f = 0.3$ if no value provided).

The third simulation (DR3-run) contained 215 clusters corresponding to the young ($< 30\,\mathrm{Myr}$) clusters from Hunt & Reffert [35] that overlap with the sample of Celli et al. [45]. Metallicities and binary fractions were again taken from Almeida et al. [44], with primary masses sampled from the Weidner & Kroupa [37] IMF over $[0.08, 150]\,\mathrm{M}_\odot$. The lower limit of secondary masses was set to $0.1\,\mathrm{M}_\odot$. The parameters and literature sources for all three runs are summarized in Tab. 4.1.

	DR2(1)-run	DR2(2)-run	DR3-run
N_c	387 [45]	387 [45]	215 [45][35]
k	Celli et al. [45]	Celli et al. [45]	Hunt & Reffert [35]
f	0	Almeida et al. [44]	Almeida et al. [44]
Z	Kharchenko et al. [46]	Almeida et al. [44]	Almeida et al. [44]
$\xi(M)$	Kroupa [43]	Weidner & Kroupa [37]	Weidner & Kroupa [37]
M_1	$[5, 150]\,\mathrm{M}_\odot$	$[0.08, 150]\,\mathrm{M}_\odot$	$[0.08, 150]\,\mathrm{M}_\odot$
$M_2^{\min}$	$0.05\,\mathrm{M}_\odot$	$0.08\,\mathrm{M}_\odot$	$0.1\,\mathrm{M}_\odot$

Tab. 4.1: COMPAS simulation runs and their input parameters. N_c: number of simulated clusters, k: IMF normalization factor, f: binary fraction, Z: metallicity, $\xi(M)$: initial mass function, M_1: primary star mass range, $M_2^{\min}$: secondary star mass lower limit. If no metallicity was given, solar metallicity was assumed. If no binary fraction was given, $f = 0.3$ was set.

4.2 Modeling Westerlund 1, Westerlund 2 & NGC 3603

Before analysing the simulation of a large cluster sample, first, it is informative to examine the simulation of well-studied clusters. That way we can understand how the behaviour of COMPAS depends on the chosen input parameters. This section therefore presents a detailed analysis of three of the most massive clusters in the DR2(1) and DR2(2) samples, Westerlund 1, Westerlund 2 and NGC 3603.

4.2.1 Westerlund 1: HR diagram & different metallicities

Westerlund 1 (Wd1) is one of the most massive young clusters in the Milky Way, with an estimated total stellar mass of $\sim 5 \cdot 10^4\,\mathrm{M}_\odot$ [47]. It is especially interesting for studies of massive star evolution, since it hosts WR stars, supergiant and hypergiants, LBV stars and OB supergiants [48][49]. However, the exact age of Wd1 still underlies an uncertainty, with estimates ranging from 4 to 10 Myr [49].

From the DR2 normalization factor, the total number of stars contained in Wd1 between 0.08 and $150\,\mathrm{M}_\odot$ was calculated to be 44 260, of which 20% were simulated with COMPAS. The resulting HR diagrams for a fraction of the simulated stars are shown in Fig. 4.3. Both the DR2(1) and DR2(2)-runs were performed at solar metallicity and recorded up to the age of 8 Myr. The different mass ranges of the IMF in each run are clearly reflected in these diagrams. The DR2(2) HR diagram contains a large population of low-mass stars, which evolve slowly and remain near the MS. The DR2(1) diagram, however, contains much more massive stars, which leave the MS sooner and evolve to later stages much faster.

Castellanos et al. [50] obtained infrared spectra of 110 OB stars in Wd1 to reconstruct the cluster's MS. They estimated the age from the turn-off point to be 5.5 ± 1.0 Myr. Fig. 4.4 compares their observational HR diagram to the simulated stars from the COMPAS DR2(2)-run at 4.5 Myr, 5.5 Myr and 6.5 Myr. The simulated data agrees well with the observations along the MS, although stars in the upper-right region of the HR diagram appear slightly more luminous, and stars in the upper-left region, corresponding to the literature WR stars, appear at somewhat higher effective temperatures. Since the simulation includes only 20% of the estimated stellar population, the simulated diagram naturally contains fewer stars than the observational one. After rescaling the

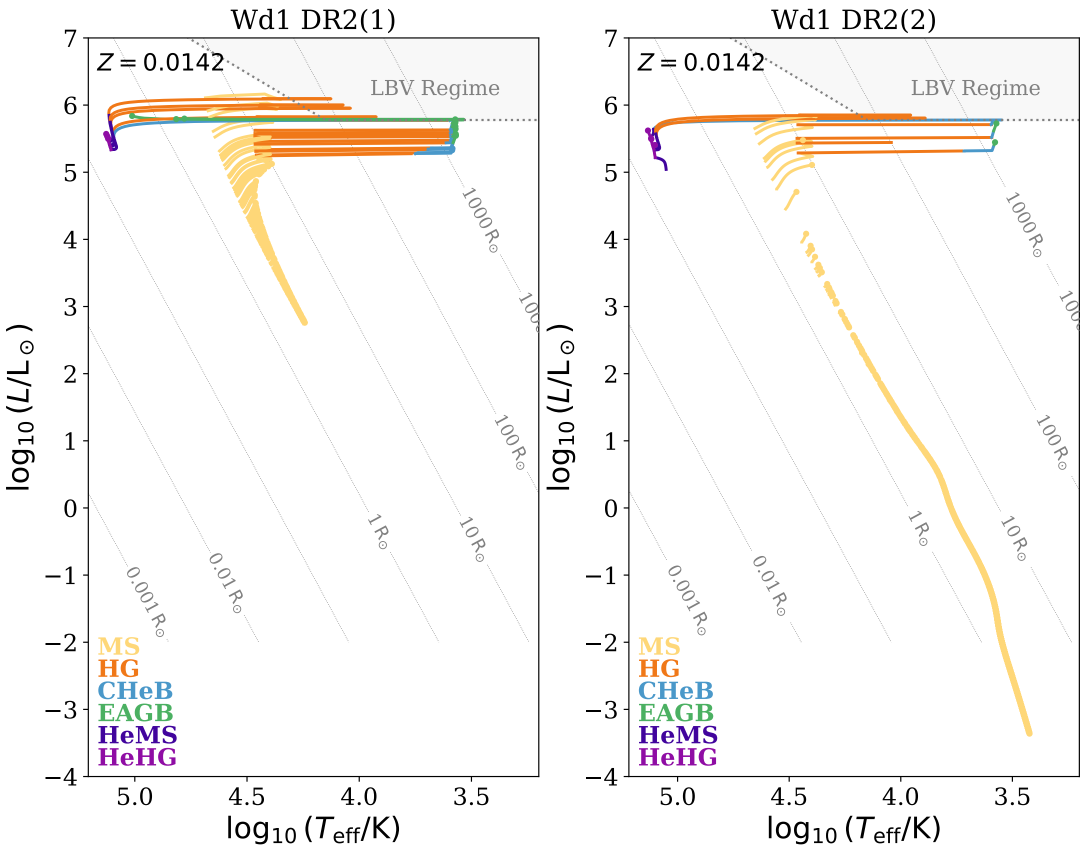

Fig. 4.3: Evolutionary tracks of stars in Westerlund 1 from DR2(1) (left) and DR2(2) (right) at solar metallicity until the age of 8 Myr. MS = Main Sequence, HG = Hertzsprung gap, CHeB = Core Helium Burning, EAGB = Early Asymptotic Giant Branch, HeMS = Helium Main Sequence, HeHG = Helium Hertzsprung Gap. For the sake of clarity, only a fraction of 2.5% of the simulated stars in DR2(1) are shown in the plot, for DR2(2) 25%.

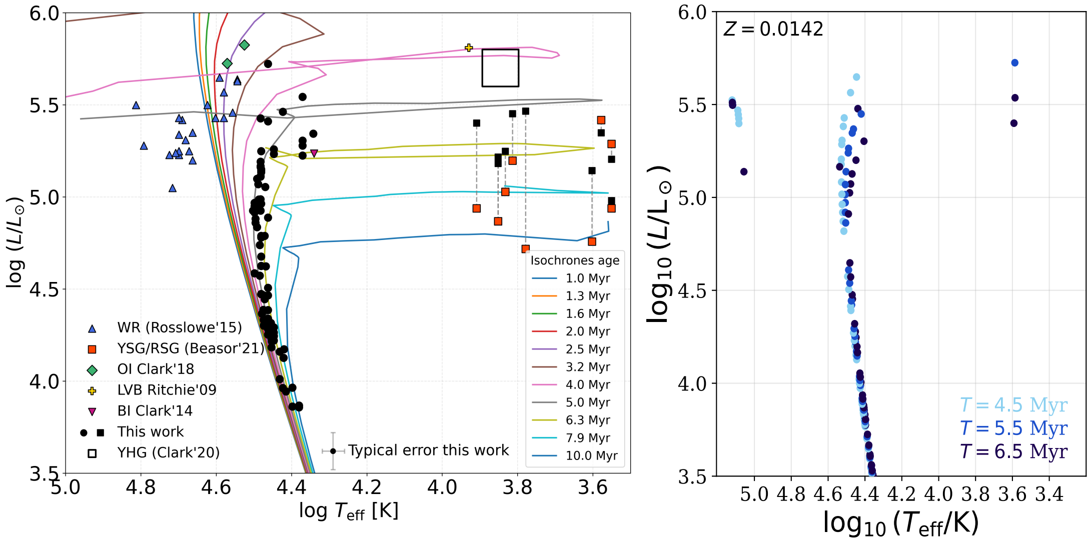

Fig. 4.4: Left: HR diagram of Wd1 as in Fig. 5 of Castellanos et al. [50]. Black circles mark the ~ 110 OB stars analysed in their work, other symbols (see legend) denote evolved members from the literature. Right: HR diagram of Wd1 in the DR2(2)-run, shown at 4.5 Myr, 5.5 Myr and 6.5 Myr.

stellar counts to the full predicted population, the simulation predicts 30 WR stars at 5.5 Myr, 25 at 4.5 Myr and 35 at 6.5 Myr. Given that Crowther et al. [48] report 24 observed WR stars in Wd1, this favours the younger end of the age estimate for Wd1.

To investigate how metallicity affects the evolution of a simulated cluster, Wd1 was additionally simulated at four metallicity values, varying from solar by $\pm 10\%$ and $\pm 50\%$. For this set of runs the binary fraction was set to $f = 0$, primary masses were drawn from a Kroupa [43] IMF, and both primary and secondary minimum masses were set to $0.08\,\mathrm{M}_\odot$. As before, 20% of the 44 260 predicted stars were simulated. Fig. 4.5 shows the resulting HR diagrams for $1Z_\odot$, $0.5Z_\odot$ and $1.5Z_\odot$ over the luminosity range $\log_{10}(L/\mathrm{L}_\odot) \in [3.5, 6.5]$. Although the evolutionary tracks shift slightly between the three metallicities, no significant overall change is visible. While stars with higher metallicities are expected to evolve faster off the MS, this is only weakly visible in the $1.5\,\mathrm{Z}_\odot$ case. Metallicity is also expected to affect the wind mass-loss rate via a power-law $\dot{M}_{\text{wind}} \propto Z^m$ [32]. This implies that stars with higher metallicities should lose more mass over their lifetimes and end up less massive. This effect should be reflected in the total cluster. The values obtained from Wd1 (see Tab. 4.2) show this trend only partially. The $0.5\,\mathrm{Z}_\odot$ cluster mass does exceed the value at $1.5\,\mathrm{Z}_\odot$ as expected, however, the remaining values show no clear power-law relation. The same is true for the wind mass-loss rate and wind luminosity[4]. The $1.5\,\mathrm{Z}_\odot$ values are significantly higher than the others. Contrary to expectation, that trend is not reflected by a correspondingly higher number of WR stars.

[4] the determination method of wind luminosities will be discussed in detail in chapter 4.3.2

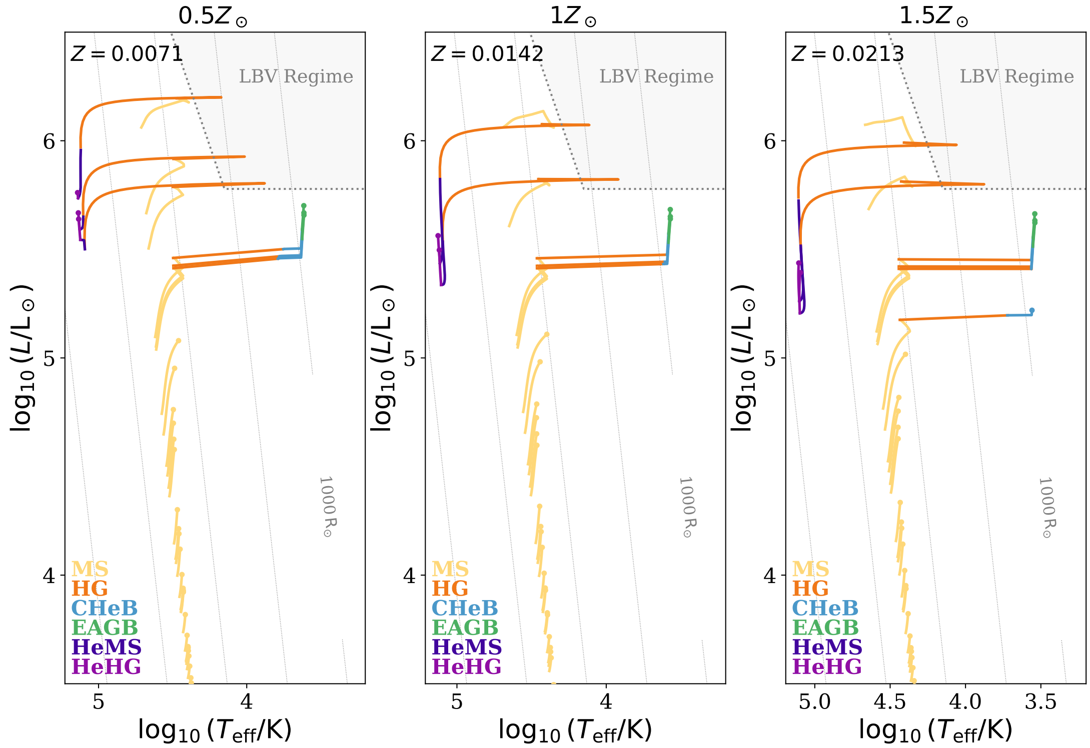

Fig. 4.5: HR diagrams of Westerlund 1 simulated with different metallicities: $1Z_\odot$ (middle), $0.5Z_\odot$ (left), $1.5Z_\odot$ (right). The HR diagram is limited to a range of $\log_{10}(L/\mathrm{L}_\odot) \in [3.5, 6.5]$

$Z(\mathrm{Z}_\odot)$	$M_c(10^3\mathrm{M}_\odot)$	$\dot{M}_{\rm wind}(10^{-6}\mathrm{M}_\odot/\mathrm{yr})$	$L_w(10^{40}\mathrm{erg/s})$	SNe	WR
0.5	18.54	1.96	5.40	45	30
0.9	18.16	1.91	5.25	35	20
1	18.19	1.95	5.20	30	15
1.1	18.28	1.88	5.20	40	20
1.5	18.19	9.00	20.5	35	15

Tab. 4.2: Cluster values evaluated for Westerlund 1 with different metallicities Z at an age of 7.9 Myr. M_c: cluster mass, $\dot{M}_{\rm wind}$: wind mass loss rate, L_w: wind luminosity, SNe: number of supernovae, WR: number of Wolf-Rayet stars

4.2.2 Cluster mass & mass distribution

Now, let us focus on the cluster mass and its distribution: The simulated cluster masses compared to those of Celli et al. [45] are shown in Tab. 4.3. The DR2(1)-run predicts values approximately 15 times higher that the values of Celli et al. [45], while the DR2(2)-run predicts masses $\sim 20\%$ lower than the literature values. The overestimate in the DR2(1)-run can be explained by the initial parameter choices and the resulting mass distribution (see Fig. 4.6). Since primary masses were drawn from the mass interval $[5, 150]\,\mathrm{M}_\odot$, the DR2(1) mass distribution peaks near $\log_{10}(5) \approx 0.7$. Masses below $5\,\mathrm{M}_\odot$ are reached only through secondary stars via $M_{2,i} = q_i \cdot M_{1,i}$, with a lower limit of $0.05\,\mathrm{M}_\odot$. As a result, intermediate- and high-mass stars are much more abundant than low-mass stars. The resulting distribution is not following a Kroupa IMF and therefore systematically overestimates the cluster mass. This is not the case in the DR2(2)-run. Here the primary mass range extends down to $0.08\,\mathrm{M}_\odot$ and secondary masses have a hard lower limit of $0.08\,\mathrm{M}_\odot$. In this case, the mass distribution follows the expected Weidner & Kroupa [37] IMF slopes. At an age of 7.9 Myr, the number of massive stars decreases in both simulations, showing a cut-off near $\log_{10}(M/\mathrm{M}_\odot) \approx 1.4$. The DR2(2)-run represents the expected mass distribution better than the DR2(1)-run and therefore reproduces cluster masses more precisely compared to the literature.

Cluster	T_{age} [Myr]	M_c [$10^3\mathrm{M}_\odot$] DR2(1)	DR2(2)	Celli
Wd 1	7.9	322	19	22.2
Wd 2	4.0	35	1.7	2.2
NGC 3603	1.0	83	3.7	4.8

Tab. 4.3: Comparison of the cluster masses of three clusters from different COMPAS runs to the values provided by Celli et al. [45] at the indicated cluster ages T_{age}.

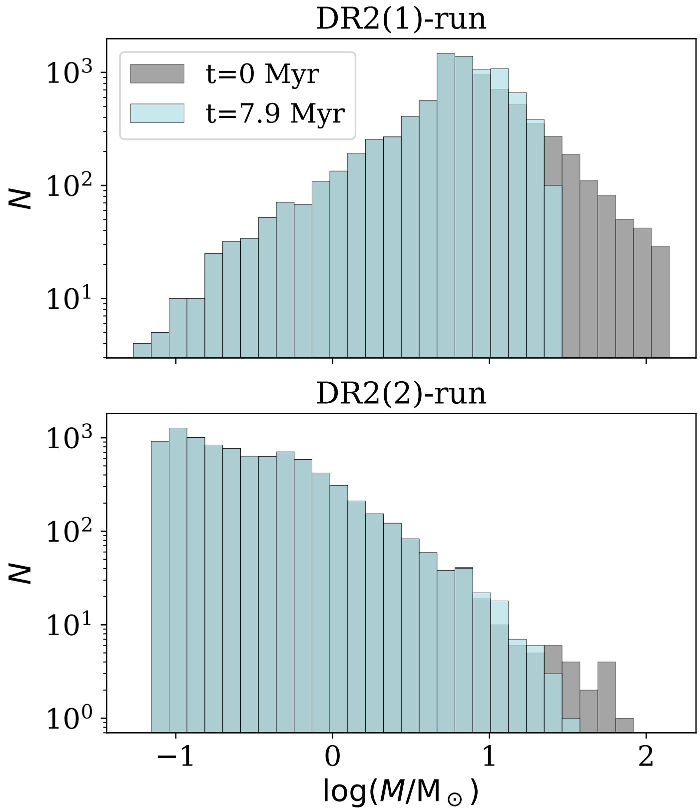

Fig. 4.6: Mass distribution of Wd1 in the DR2(1) and DR2(2)-run. IMF ranging from $[5, 150]\,\mathrm{M}_\odot$ for DR2(1)-run and $[0.08, 150]\,\mathrm{M}_\odot$ for DR2(2)-run. Masses of secondary stars are calculated by $M_{2,i} = q_i \cdot M_{1,i}$ with $q_i \in [0.01, 1]$ and a set lower limit at $0.08\,\mathrm{M}_\odot$ for DR2(2). The initial mass distribution ($t = 0$) is shown in grey, the mass distribution at a cluster age of $t = 7.9\,\mathrm{Myr}$ is shown in turquoise.

4.2.3 HR diagram of simulated clusters

Similar to Fig. 2.5, the simulated clusters can also be plotted together in a single HR diagram to compare their ages. Fig. 4.7 shows a snapshot of selected clusters from the DR2(2)-run at their current ages (following Celli et al. [45]). As expected, the position of the turn-off point shifts with cluster age. For older clusters such as NGC 663, the most massive stars have already left the MS, which shifts the turn-off to lower masses. For younger clusters such as NGC 3603, the turn-off remains near the upper end of the MS, where massive stars are only just beginning to evolve away from it.

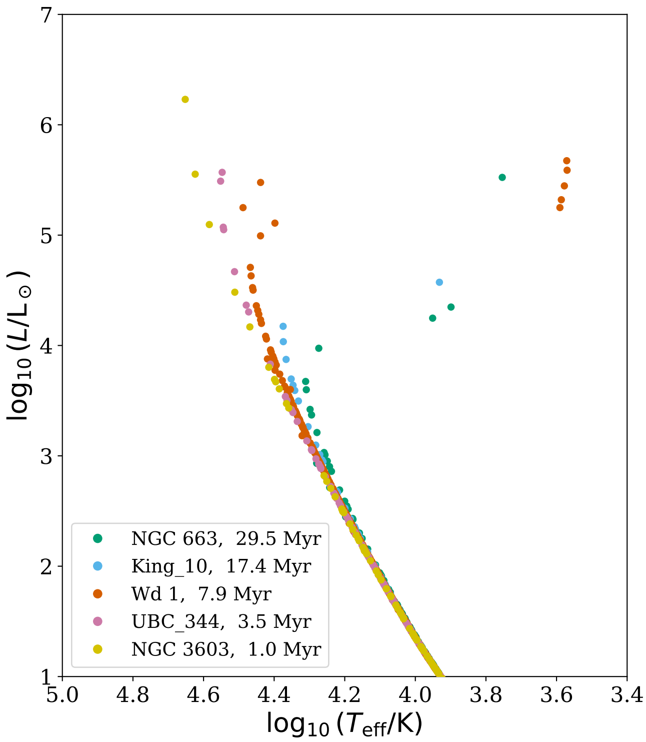

Fig. 4.7: HR diagram of selected clusters of the DR2(2)-run at their current ages.

4.3 Simulated Clusters from *Gaia* DR2 & DR3

4.3.1 Comparing cluster masses to literature

Finally, to test the overall consistency of the simulations, the whole set of simulated clusters is compared to literature values. Cluster masses from the simulations are compared to three different *Gaia*-based catalogues (Celli et al. [45], Almeida et al. [44] and Hunt & Reffert [35]) and one pre-*Gaia* catalogue (Piskunov et al. [51]). The resulting comparisons are shown in Fig. 4.8, with the respective common sample size listed in Tab. 4.4.

The different methods of the *Gaia*-based catalogues have been described in chapter 4.1. Piskunov et al. [51] (see also [52] and [53]) were among the first to determine the masses for a large sample of pre-*Gaia* open clusters. They used two independent methods to derive cluster masses: profile fitting techniques (deriving cluster masses from cluster radii) and semi-major axes fitting. The comparison between the three COMPAS runs and masses from the profile fitting method is shown in the bottom row of Fig. 4.8. The shared sample size contains 38 cluster for the DR2(1)-run and 33 clusters for the DR2(2)-run. The masses determined by Piskunov et al. [51] depend highly on the member star catalogue they used and the resulting cluster radii. Since their catalogue differs from the one used for the COMPAS simulations, this causes large discrepancy between simulated and literature masses from Piskunov et al. [51].

	DR2	**DR3**
Celli et al. [45]	387	215
Hunt & Reffert [35]	311	215
Almeida et al. [44]	101	71
Piskunov et al. [51]	38	33

Tab. 4.4: Common cluster samples of DR2 and DR3-based COMPAS runs with the literature.

The simulated masses correlate the most with the mass estimates from Celli et al. [45]. The maximum Pearson correlation coefficients[5] were achieved when comparing the DR2(1) and DR2(2)-run to Celli et al. [45] ($r \approx 0.99$ and $r \approx 0.97$, respectively). The correlation between the DR3-run and Celli et al. [45] is somewhat weaker ($r \approx 0.77$). This was expected since the DR3-run is normalized using the Hunt & Reffert [35] DR3-based catalogue rather than the DR2-based Celli et al. [45] data. Comparing the two DR2-based runs directly, the DR2(1)-run systematically overestimates the literature masses for most of the clusters. This is a consequence of its IMF bounds, which biases the resulting mass distribution to high-mass stars, as demonstrated in chapter 4.2.2.

For the DR3-run, simulated cluster masses correlate the most with the values of Hunt & Reffert [35] ($r \approx 0.95$). This follows from the fact that the IMF normalization of the DR3-run is derived from the Hunt & Reffert [35] member catalogue. Nonetheless, COMPAS systematically predicts higher cluster masses, especially for the most massive clusters. This trend is observed across all DR3-run comparisons. It suggests that either COMPAS is overestimating individual stellar masses, or that the simulation predicts a large amount of stars that are not considered in the literature.

The mass estimates of Almeida et al. [44] and Celli et al. [45] are generally lower than those of Hunt & Reffert [35]. This can be explained by the fact that they do not apply additional corrections to the *Gaia* data as Hunt & Reffert [35] does. In general, differences between observed and simulated cluster masses may be caused by the chosen mass function, the method used to extrapolate unobserved mass ranges, or differences between the cluster member catalogues. The full set of correlation coefficients is given in Tab. A.1. The cluster masses of the three simulations can be found in Tab. A.4, Tab. A.5 and Tab. A.6 for the ten most massive clusters in each COMPAS run, or at `https://github.com/annarose-22/modeling-stellar-clusters` for all clusters.

[5]The Pearson correlation coefficient r quantifies the linear correlation between two datasets on a scale from -1 (perfect negative correlation) to 1 (perfect positive correlation), with 0 representing no correlation.

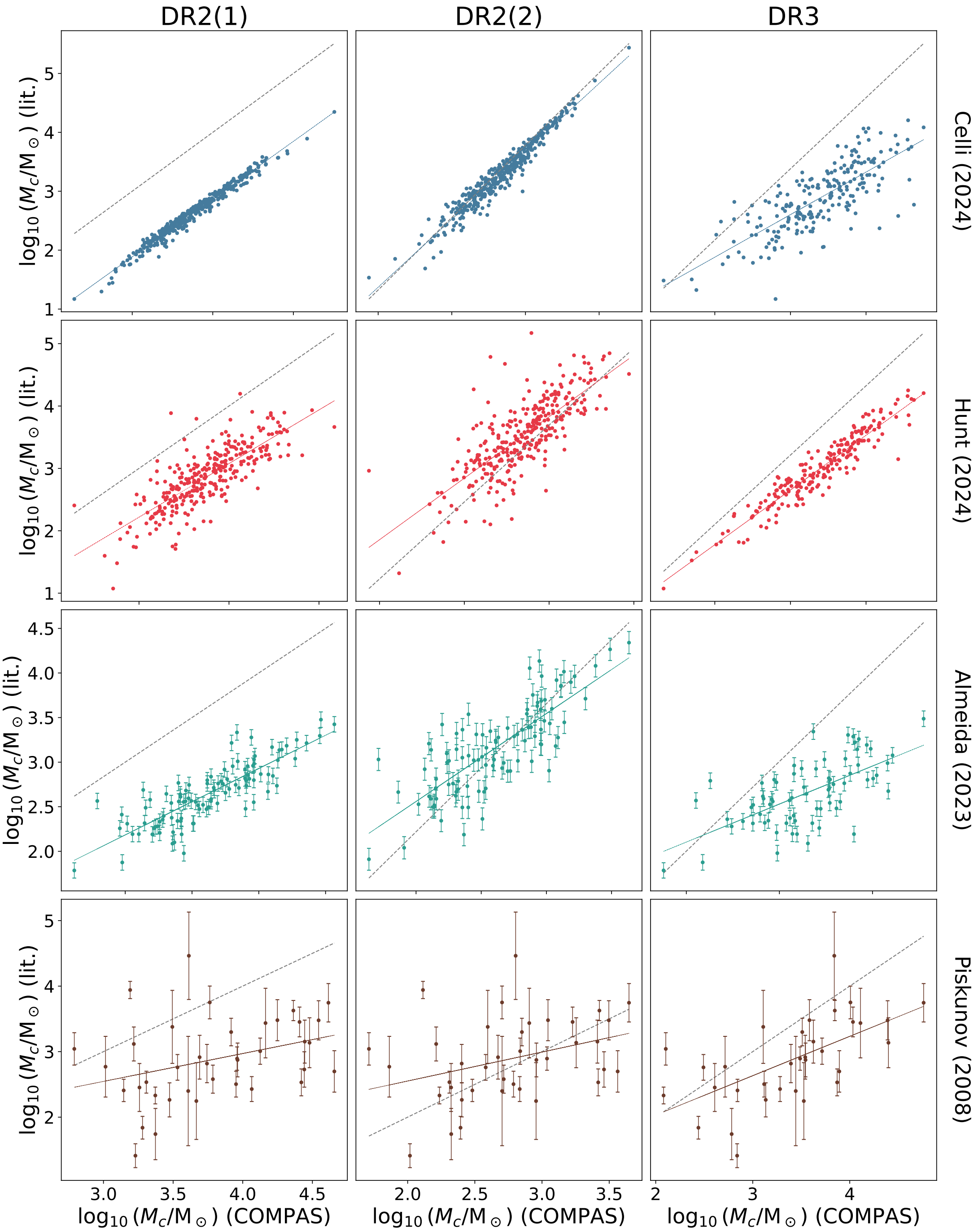

Fig. 4.8: Comparing stellar cluster masses M_c of different COMPAS runs to those in the literature (Celli et al. [45], Hunt & Reffert [35], Almeida et al. [44], Piskunov et al. [51]). The x-axes show values from this work and the y-axes show the cluster masses of the respective literature. The grey dashed lines mark the identity of COMPAS and literature values.

4.3.2 Wind mass-loss rates & wind luminosity

Since the COMPAS output does not directly provide stellar wind speed, it is computed using the empirical description adopted by Celli et al. [45], based on Kudritzki & Puls [54]. For a single star, the wind speed is given by

$$v_{w,s} = C(T_{\text{eff}}) \cdot \sqrt{\frac{2GM}{R_s} \cdot \left(1 - \frac{L_s}{L_{\text{Edd}}}\right)}\ , \tag{4.2}$$

where R_s is the stellar radius, L_s the stellar luminosity and $L_{\text{Edd}} = 4\pi G m_p M c/\sigma_T$ the Eddington luminosity, with the proton mass m_p and the Thomson cross section σ_T. The multiplicative factor $C(T_{\text{eff}})$ depends on effective temperatures as

$$C(T_{\text{eff}}) = \begin{cases} 1.0 & T_{\text{eff}}/K < 10^4 \\ 1.4 & 10^4 \leq T_{\text{eff}}/K < 2.1 \cdot 10^4 \\ 2.65 & T_{\text{eff}}/K \geq 2.1 \cdot 10^4\ . \end{cases} \tag{4.3}$$

To avoid discontinuities at the temperature boundaries, linear interpolation is applied between $C = 1$ and $C = 2.65$, following Celli et al. [45]. The cluster wind speed follows from momentum conservation and summing over the wind-mass loss rates $\dot{M}_s$ of all simulated binary system:

$$\dot{M}_c v_{w,c} = \sum_i \dot{M}_{s,i} v_{w,s,i}\ , \tag{4.4}$$

with the total cluster wind mass-loss rate $\dot{M}_c = \sum_i \dot{M}_{s,i}$. Since each binary system contains two stars, this becomes

$$v_{w,c} = \frac{\sum_i [\dot{M}_{1,i} v_{1,i} + \dot{M}_{2,i} v_{2,i}]}{\sum_i [\dot{M}_{1,i} + \dot{M}_{2,i}]}\ , \tag{4.5}$$

with i running over all simulated binary systems. The cluster wind luminosity then follows as:

$$L_{w,c} = \frac{1}{2} \dot{M}_c v_{w,c}^2\ . \tag{4.6}$$

Stars for which the wind velocity is undefined (such as compact remnants with vanishing radii, or stars exceeding the Eddington limit) are excluded from the cluster wind calculation. The stellar parameters that are required to evaluate the wind luminosity (mass, radius, luminosity, effective temperature, and wind mass-loss rate) are obtained from interpolation like in chapter 3.3.

Wind mass-loss rates and wind luminosities for the three COMPAS runs compared to the values by Celli et al. [45] are shown in Fig. 4.9. For the DR2(1)-run both distributions have standard deviations comparable to those of Celli et al. [45]. However, they are shifted to systematically higher values overall. Celli et al. [45] report median values of $1.3 \cdot 10^{-8}\,\mathrm{M}_\odot/\mathrm{yr}$ for the wind mass-loss rate and $3 \cdot 10^{34}\,\mathrm{erg/s}$ for the wind luminosity. The median values of the simulations are $1 \cdot 10^{-5}\,\mathrm{M}_\odot/\mathrm{yr}$ and $3 \cdot 10^{41}\,\mathrm{erg/s}$ for $\dot{M}_{\text{wind}}$ and L_w, respectively.

In the DR2(2)-run, the simulated median values are slightly lower than the Celli et al. [45] values ($3 \cdot 10^{-9}\,\mathrm{M}_\odot/\mathrm{yr}$ and $6 \cdot 10^{33}\,\mathrm{erg/s}$), and the standard deviations differ more

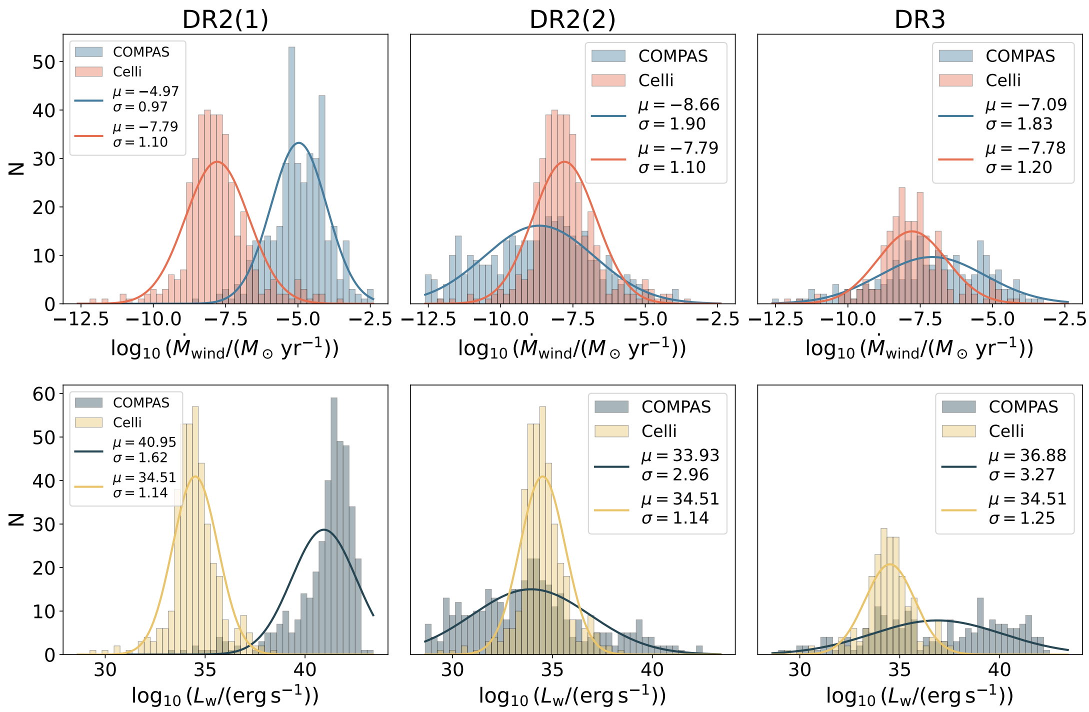

Fig. 4.9: Comparison of wind mass-loss rates $\dot{M}_{\rm wind}$ and wind luminosities L_w from COMPAS DR2(1), DR2(2) and DR3-runs to Celli et al. [45]. Solid lines show Gaussian fits with standard deviation σ and peak position μ indicated in the legend. For DR2(1) and DR2(2) the sample of 387 clusters is shown, for DR3, the common sample of 215 cluster is shown.

significantly. The broader distribution compared to DR2(1) may be caused by the non-zero binary fraction, which was the second major change besides the IMF bounds.

In the DR3-run, the smaller sample of 215 clusters shows a broader distribution as well, but with slightly higher medians ($1.2 \cdot 10^{-7}\,\mathrm{M_\odot/yr}$ and $1.4 \cdot 10^{47}\,\mathrm{erg/s}$). Since the DR3-run simulates more stars than considered in the DR2-based method of Celli et al. [45], the resulting distribution is shifted to higher values.

Another factor playing into the discrepancy of simulated and observed data is that Celli et al. [45] assumed solar metallicity throughout their calculations. As described in chapter 4.2.1, the wind mass-loss rate, and therefore, wind luminosity depend on metallicity [55]. Celli et al. [45] estimate that an increase of $\sim 50\%$ in cluster metallicity would raise the total wind luminosity by roughly 40%. Since for the COMPAS simulations metallicities were assigned based on observational catalogues, many clusters were evolved with a metallicity different from the solar metallicity. This likely contributes to the discrepancy with the values of Celli et al. [45].

4.3.3 Supernovae & Wolf-Rayet star counts

Supernova events are recorded in separate files of the COMPAS output. The number of SNe per cluster can simply be obtained by counting the recorded events in these files. The resulting SN count distributions for the three COMPAS runs are shown in the upper row of Fig. 4.10 (turquoise). The corresponding SN counts from Celli

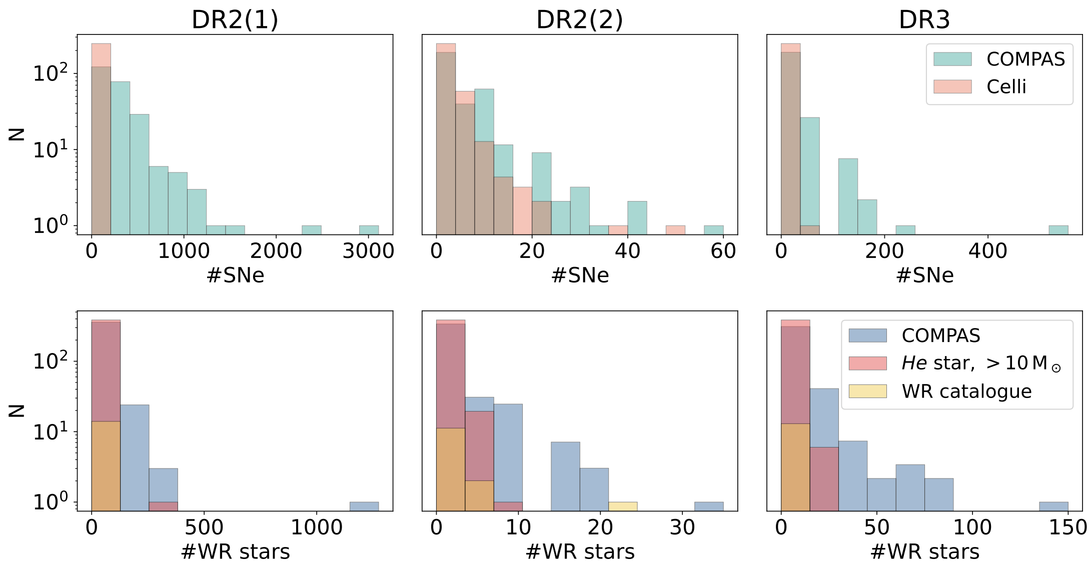

Fig. 4.10: Upper row: Number of SNe for the three COMPAS runs compared to the SNe counts from Celli et al. [45]. Lower row: Number of WR stars identified via dominant mass-loss rate (blue) and via selection of stars $> 10\,\mathrm{M}_\odot$ with stellar types 7, 8 or 9 (naked He stars) (red). WR counts from [56] are shown in yellow.

et al. [45] are shown in pink. To estimate the number of SNe, Celli et al. [45] counted the number of stars within the mass range $[M_{\max,0}, M_{\max}(T_{\mathrm{age}})]$, where $M_{\max,0}$ is the highest stellar mass ever present in the cluster and $M_{\max}(T_{\mathrm{age}})$ the maximum mass that is expected to remain at the current cluster age. COMPAS overestimates the number of SNe in the DR2(1)-run (notice the different scaling of the x-axes), consistent with its overestimation of cluster mass. The DR2(2)-run agrees better with the data from Celli et al. [45], however, COMPAS still predicts slightly higher SN counts.

To identify the number of WR stars in the simulations, the "dominant-mass-loss-rate" output parameter is used. It records a star's dominant mass-loss mechanism at each time step. Stars flagged with the dominant mass-loss rate classified as Wolf-Rayet at the cluster's current age are assumed to be WR stars. The distributions of WR star counts are shown in blue in the lower row of Fig. 4.10.

An alternative method (shown in red) classifies stars as WR stars if they satisfy two conditions: (a) stellar type of 7 (Naked Helium Star MS), 8 (Naked Helium Star Hertzsprung Gap) or 9 (Naked Helium Star Giant Branch), and (b) a mass exceeding $10\,\mathrm{M}_\odot$. These conditions are chosen according to the classification of WR stars in chapter 2.2.2. WR stars from the observational GaiaDR3 [56] catalogue are shown in yellow for comparison. Across all three COMPAS simulations, the predicted WR counts exceed those of the observational catalogue by several orders of magnitude, regardless of which identification criterion is used. This suggests that either the evolution models used in COMPAS tends to overestimate the wind mass-loss rates of massive stars, which then are wrongly counted as WR stars, or that the observed WR catalogue is not accounting for all existing WR stars. Since WR stars contribute significantly to the wind mass-loss of a cluster, overestimates of WR stars are linked to the estimates of the wind properties.

5 Conclusion & Outlook

This thesis analysed the properties of young stellar clusters simulated with the BPS code COMPAS. Three major simulation runs were performed differing in their IMF mass ranges, metallicities and binary fractions. Also, different observational cluster catalogues were used to normalize the IMF. The obtained results were then compared to *Gaia*-based and pre-*Gaia* observational catalogues.

It was found that the IMF mass range has a significant impact on the cluster masses. The DR2(1)-run, which sampled primary masses only in $[5, 150]\,\mathrm{M}_\odot$, systematically overestimated cluster masses by a factor of ~ 15 relative to Celli et al. [45], since the mass distribution is biased towards higher stellar masses. Extending the IMF down to $0.08\,\mathrm{M}_\odot$ in the DR2(2)-run resolved this issue, where cluster mass values lie within $\sim 20\%$ of the literature. The correlation between simulation and literature was the highest for Celli et al. [45] in both DR2 runs ($r \approx 0.99$ and $r \approx 0.97$), since the simulation input was based on their normalization factors. The DR3-run correlates best with Hunt & Reffert [35] ($r \approx 0.95$) for the same reason. However, cluster masses are still systematically overestimated for massive clusters. Comparison to the pre-*Gaia* catalogue (Piskunov et al. [51]) showed the lowest correlation ($r \approx 0.35$ for the DR2(2)-run). Wind mass-loss rates and wind luminosities, as well as supernova and Wolf-Rayet star counts follow the same trends as the cluster masses. Overall, the results show that cluster simulations based on COMPAS can reproduce the qualitative trends of observed clusters, but quantitative agreement is highly sensitive to the choice of IMF bounds, the cluster catalogue used for normalization, and corrections for observational data.

Since the stellar clusters were constructed using binary population synthesis, gravitational effects between the binary systems are neglected. However, an additional gravitational force between stars systems has an impact on the evolution of stellar clusters as well [57]. Apart from that, the prescriptions used in COMPAS underlie certain uncertainties themselves, affecting mostly the evolution of high mass stars, which have a large impact on the cluster mass and wind properties. In addition to that, COMPAS is using extrapolated models of Pols et al. [41] for very high mass stars, which adds to the uncertainty of their evolution.

Most BPS codes, including COMPAS, predict stellar mass-loss rates, but not explicitly wind velocities. Therefore, the wind luminosity had to be derived from additional empirical prescriptions. SPS codes such as pyStarburst99 [58], SLUG [59] or the Geneva code [60] provide both wind luminosity and velocity. They are therefore more suitable for studies of cluster wind properties.

Estimating the mass of stellar clusters remains a challenge in astrophysics, but plays an important role in the search of possible particle accelerators. Future work could improve on the limitations of the methods in this work in several ways. For example, the gravitational effects between star systems could be taken into account via N-body codes. Also, with future *Gaia* data releases (DR4 scheduled at the end of 2026, and DR5 in 2030) the observational cluster catalogues likely will be updated to larger and more reliable cluster samples. Repeating this comparison with updated observational data will help to identify whether the discrepancies originate primarily from the simulation method, the stellar evolution prescriptions, or the remaining incompleteness of the observations.

A Appendix A

Tab. A.1: Pearson correlation factors r between the COMPAS simulations DR2(1), DR2(2) and DR3 and literature values.

	DR2(1)	**DR2(2)**	**DR3**
Celli et al. [45]	0.99	0.97	0.77
Hunt & Reffert [35]	0.79	0.76	0.95
Almeida et al. [44]	0.83	0.79	0.64
Piskunov et al. [51]	0.43	0.35	0.61

Tab. A.2: Information about columns provided in the cluster data.

Column	Unit	Description
Cluster	–	Cluster name, according to Gaia DR2 label
Age	Myr	Cluster age
k	–	Normalization of the IMF
N	–	Number of cluster members
N_{sys}	–	Number of binary systems simulated
Z	–	Cluster metallicity
f_{bin}	–	Binary fraction adopted in the simulation
M_{c}	$M_{\odot}$	Cluster mass
$\dot{M}$	$M_{\odot}\,\mathrm{yr}^{-1}$	Cluster wind mass loss rate
SNe	–	Number of supernova explosion by the cluster age
WR	–	Number of stars with dominant Wolf-Rayet mass-loss
WR2	–	Number of WR stars identified from stellar type and mass
L_{w}	W	Cluster wind luminosity

Tab. A.3: Information about columns provided in the tables of sampled COMPAS input parameters.

Column	Unit	Description
Cluster	–	Parent cluster name
a	AU	Initial binary semi-major axis
M_1	$M_{\odot}$	Primary star mass
M_2	$M_{\odot}$	Secondary star mass

Note. Data tables are available at
`https://github.com/annarose-22/modeling-stellar-clusters`

Tab. A.4: Data of the 10 largest stellar clusters from the COMPAS DR2(1)-run

Cluster	T_{age} (Myr)	N	Z	M_c ($M_\odot$)	$\dot{M}$ ($M_\odot\,\mathrm{yr}^{-1}$)	L_w (W)	SNe	WR	WR2
Westerlund_1	7.9	42850	0.0142	3.227e+05	9.10e-04	2.58e+36	3110	1275	340
Danks_2	2.0	13760	0.0142	1.481e+05	2.60e-03	4.52e+32	0	0	0
NGC_3603	1.0	8540	0.0142	8.370e+04	1.13e-03	2.76e+32	0	0	0
NGC_663	29.5	8135	0.0142	4.121e+04	3.44e-05	9.85e+34	2445	290	40
Danks_1	1.0	7755	0.0142	8.462e+04	1.46e-03	3.52e+32	0	0	0
NGC_869	15.1	7440	0.0142	4.621e+04	2.54e-04	9.30e+35	1140	245	70
UBC_344	3.5	6745	0.0142	6.513e+04	4.00e-03	4.66e+32	0	45	45
Patchick_94	3.5	6715	0.0142	6.411e+04	2.78e-03	2.84e+32	0	25	25
NGC_4755	12.0	6540	0.0142	4.424e+04	1.97e-04	5.60e+35	840	245	55
NGC_6231	13.8	6425	0.0142	4.091e+04	2.20e-04	6.20e+35	975	225	50

Tab. A.5: Data of the 10 largest stellar clusters from the COMPAS DR2(2)-run

Cluster	T_{age} (Myr)	N	Z	M_c ($M_\odot$)	$\dot{M}$ ($M_\odot\,\mathrm{yr}^{-1}$)	L_w (W)	SNe	WR	WR2
Westerlund_1	7.9	44260	0.0142	2.543e+04	1.81e-05	3.99e+34	60	35	10
Danks_2	2.0	14213	0.0142	8.764e+03	5.05e-06	1.22e+30	0	0	0
NGC_3603	1.0	8820	0.0142	5.172e+03	1.23e-04	2.72e+31	0	0	0
NGC_663	29.5	8402	0.0142	4.440e+03	1.56e-06	3.46e+27	5	0	0
Danks_1	1.0	8010	0.0142	4.461e+03	6.80e-07	1.77e+29	0	0	0
NGC_869	15.1	7686	0.0142	3.983e+03	3.09e-08	2.14e+32	30	0	0
UBC_344	3.5	6965	0.0142	4.686e+03	1.34e-05	2.11e+30	0	0	0
Patchick_94	3.5	6934	0.0142	3.854e+03	1.85e-08	3.11e+27	0	0	0
NGC_4755	12.0	6757	0.0142	3.466e+03	7.20e-08	2.04e+32	15	15	5
NGC_6231	13.8	6637	0.0142	4.714e+03	1.24e-05	8.15e+33	30	0	0

Tab. A.6: Data of the 10 largest stellar clusters from the COMPAS DR3-run

Cluster	T_{age} (Myr)	N	Z	M_c ($M_\odot$)	$\dot{M}$ ($M_\odot\,\mathrm{yr}^{-1}$)	L_w (W)	SNe	WR	WR2
NGC_663	29.5	103150	0.0142	5.774e+04	1.06e-05	5.85e+34	555	150	15
Berkeley_95	26.1	75274	0.0142	4.300e+04	3.23e-05	9.15e+34	125	55	15
Czernik_41	26.9	70204	0.0142	3.986e+04	1.71e-05	6.65e+34	145	35	0
Sher_1	18.9	63126	0.0142	3.742e+04	2.74e-05	6.90e+34	175	40	5
NGC_7510	19.5	60834	0.0092	3.541e+04	3.49e-06	1.08e+34	135	85	10
DC_5	18.5	58963	0.0142	3.645e+04	1.22e-04	2.90e+31	0	0	0
NGC_3603	7.1	58394	0.0142	3.599e+04	1.13e-04	2.85e+31	0	0	0
Teutsch_30	28.8	49596	0.0142	2.662e+04	2.43e-06	9.85e+33	225	85	25
NGC_457	22.8	45480	0.0142	2.456e+04	3.94e-06	1.68e+34	130	40	10
NGC_6318	14.8	44515	0.0142	2.624e+04	3.39e-05	1.55e+34	45	15	0

Acronyms

AGB Asymptotic Giant Branch.

BH Black Hole.

BPS Binary Population Synthesis.

BSE Binary Star Evolution.

COMPAS Compact Object Mergers: Population Astrophysics and Statistics.

DCO Double Compact Object.

EAGB Early Asymptotic Giant Branch.

ESA European Space Agency.

HB Horizontal Branch.

HG Hertzsprung Gap.

HR Hertzsprung-Russell.

IMF Initial Mass Function.

LBV Luminous Blue Variable.

LHAASO Large High Altitude Air Shower Observatory.

MS Main Sequence.

NS Neutron Star.

PN Planetary Nebula.

RGB Red Giant Branch.

SN Supernova.

SNe Supernovae.

SPS Stellar Population Synthesis.

SSE Single Star Evolution.

WD White Dwarf.

WR Wolf-Rayet.

ZAMS Zero-Age Main Sequence.

Bibliography

[1] G. Galilei. *Sidereus Nuncius (1610)*. Translated by Albert Van Helden. Octavo, University of Chicago Press Chicago Illinois, 1989.

[2] B. Chaboyer, P. Demarque, P. J. Kernan, and L. M. Krauss. “A Lower Limit on the Age of the Universe”. In: *Science* 271.5251 (Feb. 1996), pp. 957–961. DOI: 10.1126/science.271.5251.957.

[3] M. R. Krumholz, C. F. McKee, and J. Bland-Hawthorn. “Star Clusters Across Cosmic Time”. In: *ARA&A* 57 (Aug. 2019), pp. 227–303. DOI: 10.1146/annurev-astro-091918-104430.

[4] K. Haubner, M. Sasaki, A. Mitchell, G. Ponti, et al. “eROSITA X-ray analysis of the PeVatron candidate Westerlund 1”. In: *A&A* 695 (2025), A3. DOI: 10.1051/0004-6361/202451964. URL: https://doi.org/10.1051/0004-6361/202451964.

[5] LHAASO Collaboration. “An ultrahigh-energy gamma-ray bubble powered by a super PeVatron”. In: *Science Bulletin* 69.4 (2024), pp. 449–457. ISSN: 2095-9273. DOI: https://doi.org/10.1016/j.scib.2023.12.040. URL: https://www.sciencedirect.com/science/article/pii/S209592732300912X.

[6] A. Albert, R. Alfaro, C. Alvarez, J. D. Álvarez, et al. “Evidence that Ultra-high-energy Gamma Rays Are a Universal Feature near Powerful Pulsars”. In: *ApJ* 911.2, L27 (Apr. 2021). DOI: 10.3847/2041-8213/abf4dc.

[7] G. Morlino, S. Menchiari, E. Amato, and N. Bucciantini. *Contribution to Galactic cosmic rays from young stellar clusters*. 2023. URL: https://arxiv.org/abs/2310.15640.

[8] European Space Agency. *Gaia Archive*. 2026. URL: https://gea.esac.esa.int/archive/.

[9] T. Cantat-Gaudin. “Milky Way Star Clusters and Gaia: A Review of the Ongoing Revolution”. In: *Universe* 8.2 (2022). DOI: 10.3390/universe8020111. URL: https://www.mdpi.com/2218-1997/8/2/111.

[10] T. Cantat-Gaudin, F. Anders, A. Castro-Ginard, C. Jordi, et al. “Painting a portrait of the Galactic disc with its stellar clusters”. In: *A&A* 640 (Aug. 2020), A1. DOI: 10.1051/0004-6361/202038192.

[11] E. L. Hunt and S. Reffert. “Improving the open cluster census: II. An all-sky cluster catalogue with Gaia DR3”. In: *A&A* 673 (May 2023), A114. URL: http://dx.doi.org/10.1051/0004-6361/202346285.

[12] Team COMPAS, J. Riley, P. Agrawal, J. W. Barrett, et al. “Rapid Stellar and Binary Population Synthesis with COMPAS”. In: *The Astrophysical Journal Supplement Series* 258.2, 34 (Feb. 2022), p. 34. DOI: 10.3847/1538-4365/ac416c.

[13] J. C. Hansen, D. S. Kawaler, and V. Trimble. *Stellar Interiors. Physical Principles, Structure, and Evolution.* 2nd ed. Springer Science+Business Media, LLC, 2004.

[14] C. Conroy. "Modeling the Panchromatic Spectral Energy Distributions of Galaxies". In: *ARA&A* 51.1 (Aug. 2013), 393–455. ISSN: 1545-4282. URL: http://dx.doi.org/10.1146/annurev-astro-082812-141017.

[15] Z.W. Han, H.W. Ge, X.F. Chen, and H.L. Chen. "Binary Population Synthesis". In: *Research in Astronomy and Astrophysics* 20.10 (2020), p. 161. URL: https://doi.org/10.1088/1674-4527/20/10/161.

[16] K. Belczynski, V. Kalogera, F. A. Rasio, R. E. Taam, et al. "Compact Object Modeling with the StarTrack Population Synthesis Code". In: *ApJS* 174.1 (2008), p. 223. URL: https://doi.org/10.1086/521026.

[17] K. Breivik, S. Coughlin, M. Zevin, C. L. Rodriguez, et al. "COSMIC Variance in Binary Population Synthesis". In: *ApJ* 898.1 (2020), p. 71. URL: https://doi.org/10.3847/1538-4357/ab9d85.

[18] J. R. Hurley, C. A. Tout, and O. R. Pols. "Evolution of binary stars and the effect of tides on binary populations". In: *MNRAS* 329.4 (Feb. 2002), pp. 897–928. DOI: 10.1046/j.1365-8711.2002.05038.x.

[19] D. Prialnik. *An Introduction to the Theory of Stellar Structure and Evolution*. 2nd ed. Cambridge University Press, 2010.

[20] B. W. Carroll and D. A. Ostlie. *An Introduction to Modern Astrophysics*. 2nd ed. Pearson, 2014.

[21] P. Kroupa and C. Weidner. "Evidence for a fundamental stellar upper mass limit from clustered star formation, and some implications therof". In: *Proceedings of the International Astronomical Union* 1.S227 (May 2005), 423–433. URL: http://dx.doi.org/10.1017/S1743921305004837.

[22] A. J. Cannon and E. Pickering. *The Henry Draper (HD) Catalogue*. 1918.

[23] S. G. Ryan and A. J. Norton. *Stellar Evolution and Nucleosynthesis*. Cambridge University Press, 2010.

[24] R. Kippenhahn, A. Weigert, and A. Weiss. *Stellar Structure and Evolution*. 2nd ed. Springer, 2012.

[25] S. Chandrasekhar. "The Maximum Mass of Ideal White Dwarfs". In: *ApJ* 74 (July 1931), p. 81. DOI: 10.1086/143324.

[26] J. Krticka, J. Kubát, and I. Krticková. "New line-driven wind mass-loss rates for OB stars with metallicities down to 0.01 Z". In: *A&A* 702 (2025), A9. URL: https://doi.org/10.1051/0004-6361/202556234.

[27] A. A. C. Sander and J. S Vink. "On the nature of massive helium star winds and Wolf–Rayet-type mass-loss". In: *mnras* 499.1 (Oct. 2020), pp. 873–892. eprint: https://academic.oup.com/mnras/article-pdf/499/1/873/33873679/staa2712.pdf. URL: https://doi.org/10.1093/mnras/staa2712.

[28] J. Puls, J. S. Vink, and F. Najarro. "Mass loss from hot massive stars". In: *A&A Rev.* 16.3-4 (Dec. 2008), pp. 209–325. DOI: 10.1007/s00159-008-0015-8.

[29] A. S. Eddington. “The Internal Constitution of the Stars”. In: *The Scientific Monthly* 11.4 (1926), 297–303.

[30] R. M. Humphreys and K. Davidson. “Studies of luminous stars in nearby galaxies. III. Comments on the evolution of the most massive stars in the Milky Way and the Large Magellanic Cloud.” In: *ApJ* 232 (Sept. 1979), pp. 409–420. DOI: 10.1086/157301.

[31] K. Schwarzschild. *Über das Gravitationsfeld eines Massenpunktes nach der EINSTEINschen Theorie*. 1916.

[32] J. S. Vink, A. de Koter, and H. J. G. L. M. Lamers. “Mass-loss predictions for O and B stars as a function of metallicity”. In: *A&A* 369 (Apr. 2001), pp. 574–588. DOI: 10.1051/0004-6361:20010127.

[33] J. Merritt, S. Stevenson, A. Sander, I. Mandel, et al. *Implications of modern mass-loss rates for massive stars*. 2025. eprint: 2507.17052. URL: https://arxiv.org/abs/2507.17052.

[34] H.M.J. Boffin and D. Jones. “The importance of binary stars”. In: *Contributions of the Astronomical Observatory Skalnaté Pleso* 55.3 (2025), pp. 21–36. URL: https://doi.org/10.31577/caosp.2025.55.3.21.

[35] E. L. Hunt and S. Reffert. “Improving the open cluster census: III. Using cluster masses, radii, and dynamics to create a cleaned open cluster catalogue”. In: *A&A* 686 (May 2024), A42. ISSN: 1432-0746. DOI: 10.1051/0004-6361/202348662.

[36] E. E. Salpeter. “The Luminosity Function and Stellar Evolution.” In: *ApJ* 121 (Jan. 1955), p. 161. DOI: 10.1086/145971.

[37] C. Weidner and P. Kroupa. “Evidence for a fundamental stellar upper mass limit from clustered star formation”. In: *MNRAS* 348.1 (Feb. 2004), pp. 187–191. DOI: 10.1111/j.1365-2966.2004.07340.x.

[38] R. de Grijs, C. Li, and A. M. Geller. “The dynamical importance of binary systems in young massive star clusters”. In: *Proceedings of the International Astronomical Union* 12.S316 (2015), 222–227. DOI: 10.1017/S1743921315009096.

[39] J. R. Hurley, O. R. Pols, and C. A. Tout. “Comprehensive analytic formulae for stellar evolution as a function of mass and metallicity”. In: *MNRAS* 315.3 (2000), pp. 543–569. DOI: 10.1046/j.1365-8711.2000.03426.x.

[40] C. A. Tout, O. R. Pols, P. P. Eggleton, and Z. Han. “Zero-age main-sequence radii and luminosities as analytic functions of mass and metallicity”. In: *MNRAS* 281.1 (July 1996), pp. 257–262. eprint: https://academic.oup.com/mnras/article-pdf/281/1/257/18540111/281-1-257.pdf. URL: https://doi.org/10.1093/mnras/281.1.257.

[41] O. R. Pols, K.-P. Schröder, J. R. Hurley, C. A. Tout, and P. P. Eggleton. “Stellar evolution models for Z = 0.0001 to 0.03”. In: *MNRAS* 298.2 (Aug. 1998), pp. 525–536. eprint: https://academic.oup.com/mnras/article-pdf/298/2/525/3613579/298-2-525.pdf. URL: https://doi.org/10.1046/j.1365-8711.1998.01658.x.

[42] K Belczynski, T Bulik, C. L. Fryer, Ashley Ruiter, et al. "On the maximum mass of stellar black holes". In: *ApJ* 714.2 (2010), p. 1217. URL: https://doi.org/10.1088/0004-637X/714/2/1217.

[43] P. Kroupa. "On the variation of the initial mass function". In: *MNRAS* 322.2 (Apr. 2001), pp. 231–246. eprint: https://academic.oup.com/mnras/article-pdf/322/2/231/2852412/322-2-231.pdf. URL: https://doi.org/10.1046/j.1365-8711.2001.04022.x.

[44] A. Almeida, H. Monteiro, and W. S. Dias. "Revisiting the mass of open clusters with Gaia data". In: *MNRAS* 525.2 (Oct. 2023), pp. 2315–2340. DOI: 10.1093/mnras/stad2291.

[45] S. Celli, A. Specovius, S. Menchiari, A. Mitchell, and G. Morlino. "Mass and wind luminosity of young Galactic open clusters in GaiaDR2". In: *A&A* 686 (2024), A118. ISSN: 1432-0746. DOI: 10.1051/0004-6361/202348541.

[46] N. V. Kharchenko, A. E. Piskunov, E. Schilbach, S. Röser, and R.-D. Scholz. "Global survey of star clusters in the Milky Way. II. The catalogue of basic parameters". In: *A&A* 558, A53 (Oct. 2013), A53. DOI: 10.1051/0004-6361/201322302.

[47] M. Gennaro, W. Brandner, A. Stolte, and Th. Henning. "Mass segregation and elongation of the starburst cluster Westerlund 1: Mass segregation and elongation of Wd 1". In: *MNRAS* 412.4 (Feb. 2011), 2469–2488. ISSN: 0035-8711. DOI: 10.1111/j.1365-2966.2010.18068.x. URL: http://dx.doi.org/10.1111/j.1365-2966.2010.18068.x.

[48] P. A. Crowther, L. J. Hadfield, J. S. Clark, I. Negueruela, and W. D. Vacca. "A census of the Wolf–Rayet content in Westerlund 1 from near-infrared imaging and spectroscopy". In: *MNRAS* 372.3 (Nov. 2006), pp. 1407–1424. eprint: https://academic.oup.com/mnras/article-pdf/372/3/1407/2973761/mnras0372-1407.pdf. URL: https://doi.org/10.1111/j.1365-2966.2006.10952.x.

[49] L. Wei, P. C. Boyle, J. R. Lu, Matthew W. Hosek, et al. "Structure and Dynamics of the Young Massive Star Cluster Westerlund 1". In: *ApJ* 992.2 (Oct. 2025), p. 213. URL: http://dx.doi.org/10.3847/1538-4357/adfc60.

[50] R. Castellanos, F. Najarro, M. Garcia, I. Negueruela, et al. "First spectroscopic identification of the main sequence in Westerlund 1". In: *A&A* 708 (Apr. 2026), A209. DOI: 10.1051/0004-6361/202558099.

[51] A. E. Piskunov, E. Schilbach, N. V. Kharchenko, S. Röser, and Scholz, R.-D. "Towards absolute scales for the radii and masses of open clusters*". In: *A&A* 468.1 (2007), pp. 151–161. DOI: 10.1051/0004-6361:20077073. URL: https://doi.org/10.1051/0004-6361:20077073.

[52] A. E. Piskunov, N. V. Kharchenko, S. Röser, E. Schilbach, and Scholz, R.-D. "Revisiting the population of Galactic open clusters". In: *A&A* 445.2 (2006), pp. 545–565. DOI: 10.1051/0004-6361:20053764. URL: https://doi.org/10.1051/0004-6361:20053764.

[53] A. E. Piskunov, E. Schilbach, N. V. Kharchenko, S. Röser, and R.-D. Scholz. "Tidal radii and masses of open clusters". In: *A&A* 477.1 (Jan. 2008), pp. 165–172. DOI: 10.1051/0004-6361:20078525.

[54] R.-P. Kudritzki and J. Puls. "Winds from Hot Stars". In: *ARA&A* 38 (Jan. 2000), pp. 613–666. DOI: 10.1146/annurev.astro.38.1.613.

[55] J. S. Vink and A. A. C. Sander. "Metallicity-dependent wind parameter predictions for OB stars". In: *MNRAS* 504.2 (June 2021), pp. 2051–2061. DOI: 10.1093/mnras/stab902.

[56] GaiaDR3. *Galactic Wolf Rayet Catalogue*. https://pacrowther.staff.shef.ac.uk/WRcat/index.php. Aug. 2025.

[57] N. Lahén, A. Rantala, T. Naab, Christian Partmann, et al. "The formation, evolution and disruption of star clusters with improved gravitational dynamics in simulated dwarf galaxies". In: *MNRAS* (Feb. 2025). URL: http://dx.doi.org/10.1093/mnras/staf350.

[58] C. Hawcroft, C. Leitherer, O. Aranguré, John Chisholm, et al. "pySTARBURST99: The Next Generation of STARBURST99". In: *ApJS* 280.1 (Aug. 2025), p. 5. URL: http://dx.doi.org/10.3847/1538-4365/adddb6.

[59] R. L. da Silva, M. Fumagalli, and M. Krumholz. *SLUG: Stochastically Lighting Up Galaxies*. Astrophysics Source Code Library, record ascl:1106.012. June 2011.

[60] C. Georgy, A. Granada, S. Ekström, G. Meynet, et al. "Populations of rotating stars: III. SYCLIST, the new Geneva population synthesis code". In: *A&A* 566 (2014), A21. URL: http://dx.doi.org/10.1051/0004-6361/201423881.

Acknowledgements

I want to thank

- my supervisor Dr. Alison Mitchell for the weekly meetings and valuable feedback
- Team COMPAS for creating COMPAS and a very useful online documentation
- the people who took the time to proof-read my thesis
- my family for their love and support

Declaration of Originality

I, Anna Rosensaft, student registration number: 23104002, hereby confirm that I completed the submitted work independently and without the unauthorized assistance of third parties and without the use of undisclosed and, in particular, unauthorized aids. This work has not been previously submitted in its current form or in a similar form to any other examination authorities and has not been accepted as part of an examination by any other examination authority.

Where the wording has been taken from other people's work or ideas, this has been properly acknowledged and referenced. This also applies to drawings, sketches, diagrams and sources from the Internet.

In particular, I am aware that the use of artificial intelligence is forbidden unless its use an aid has been expressly permitted by the examiner. This applies in particular to chatbots (especially ChatGPT) and such programs in general that can complete the tasks of the examination or parts thereof on my behalf.

Any infringements of the above rules constitute fraud or attempted fraud and shall lead to the examination being graded "fail" ("nicht bestanden").

Place, Date

Signature